

1 The general formulation for mean annual runoff components 2 estimation and their change attribution

3 Yufen He¹, Changming Li^{1*}, Hanbo Yang^{1*}

4 1 State Key Laboratory of Hydroscience and Engineering, Department of Hydraulic Engineering,
5 Tsinghua University, Beijing 100084, China

6 *Correspondence: Changming Li (licm_13@163.com), Hanbo Yang
7 (yanghanbo@tsinghua.edu.cn)

8 Abstract

9 Estimating runoff components, including surface flow, baseflow and total runoff is essential for
10 understanding precipitation partition and runoff generation and facilitating water resource
11 management. However, a general framework to quantify and attribute runoff components is still
12 lacking. Here, we propose a general formulation through observational data analysis and
13 theoretical derivation based on the two-stage Ponce-Shetty model (named as the MPS model).
14 The MPS model characterizes mean annual runoff components as a function of available water
15 with one parameter. The model is applied over 662 catchments across China and the contiguous
16 United States. Results demonstrate that the model well depicts the spatial variability of runoff
17 components with R^2 exceeding 0.81, 0.44 and 0.80 for fitting surface flow, baseflow and total
18 runoff, respectively. The model effectively simulates multi-year runoff components with R^2
19 exceeding 0.97, and the proportion of runoff components relative to precipitation with R^2
20 exceeding 0.94. By using this conceptual model, we elucidate the responses of surface flow and
21 baseflow to available water and environmental factors for the first time. The surface flow is
22 jointly controlled by precipitation and environmental factors, while baseflow is mainly influenced
23 by environmental factors in most catchments. The universal and concise MPS model offers a new
24 perspective on the long-term catchment water balance, facilitating broader application in
25 large-sample investigations without complex parameterizations and providing an efficient tool to
26 explore future runoff variations and responses under changing climate.

27 **Key Points**

28 (1) A general and concise formulation is proposed to quantify, and attribute mean annual
29 surface flow, baseflow and total runoff.

30 (2) The formulation characterizes runoff components as a function of available water without
31 additional and complicated parameter calculation.

32 (3) The formulation performs well in quantifying and attributing runoff components in 662
33 catchments.

34 **1. Introduction**

35 Runoff is the primary freshwater resource accessible for human life and plays an essential role
36 in the water cycle (He et al., 2022; Wang et al., 2024). Based on the propagation time and
37 hydraulic response of a catchment, total runoff (Q) can be divided into baseflow (Q_b) and surface
38 flow (Q_s) (Gnann et al., 2019; Singh et al., 2019). Baseflow, also referred to as slow flow, is
39 defined as the flow that originates from groundwater and other delayed sources (such as wetlands,
40 lakes, snow and ice), and generally sustains streamflow during dry periods (Gnann, 2021; Hall,
41 1968). Baseflow is the relatively stable component of runoff, playing a vital role in aquatic
42 ecosystems (de Graaf et al., 2019; Price et al., 2011), water quality (Ficklin et al., 2016) and
43 sustained water supplies (Fan et al., 2013). Surface flow, also referred to as fast flow, results from
44 rapid processes like the saturation or infiltration of excess overland flow and swift subsurface
45 flow (Beven and Kirkby, 1979), leading to immediate water movement. Surface flow occurs more
46 rapidly and with more drastic changes than baseflow, which is primarily responsible for flood
47 generation (Yin et al., 2018) and soil erosion (Morgan, 2011).

48 Most current studies focus on total runoff variability and attribution, and the relevant
49 researches are fairly mature (Berghuijs et al., 2017; Han et al., 2023; Liu et al., 2021). However,
50 few studies pay attention to comprehensive research on the different runoff components (Li et al.,
51 2020; Liu et al., 2019), and the attributions of Q_s and Q_b changes are still unclear (Hellwig and
52 Stahl, 2018). Baseflow and surface flow represent different hydrological processes, and their
53 implications for watershed management are also not identical (Zheng Mingguo, 2014). For

example, the research conducted by Ficklin et al. (2016) in the United States points out apparent spatial differences between Q_b and Q_s in different seasons. Therefore, it is necessary to quantify runoff components and distinguish their controlling factors to better understand the runoff dynamics and facilitate water resources management in the context of intensified climate change and anthropogenic disturbance.

Unlike Q , which is ascertainable through direct observation at hydrological gauges, Q_b and Q_s can only be estimated through indirect methods, including baseflow separation (Wu et al., 2019; Zhang et al., 2017), isotope tracing (Hale et al., 2022; Wallace et al., 2021) and hydrological modeling (Al-Ghobari et al., 2020; Cheng et al., 2020; Huang et al., 2007; Kaleris and Langousis, 2017). The first two methods estimate Q_b initially, and Q_s is then derived as the difference between the Q and the estimated Q_b , limiting their ability to examine the dynamic variations of each runoff component independently, and the isotope tracing method is challenging to conduct on a large and long-term scale. The hydrological modeling enables to simulate Q_b and Q_s separately, typically reflected in different modules and empirical formulations. In hydrological models, Q_b is encoded using linear or non-linear storage-discharge functions (Chen and Ruan, 2023; Cheng et al., 2020). Q_s is closely related to rainfall, but the models for estimating it are usually event-based (such as the Soil Conservation Service Curve Number method (Al-Ghobari et al., 2020; SCS, 1972; Shi et al., 2017) and very few studies explored the controls on the mean annual Q_s (Neto et al., 2020). Among various models, the Budyko framework (Budyko, 1974) in conjunction with water-energy balance method (Choudhury, 1999; Yang et al., 2008) (see the second row in Table 1), has been widely used in the analysis of mean annual Q due to its simple, universal and transparent characteristics (He et al., 2022; Roderick and Farquhar, 2011).

Recently, utilizing the extended Budyko framework to estimate Q_b and Q_s has attracted attention. Wang and Wu (2013) and Neto et al. (2020) established the regression relationship between baseflow fraction (BFC , the ratio of Q_b to precipitation (P)) and aridity index (ϕ , the ratio of mean annual potential evapotranspiration (E_0) to P) using analytical formulation. However, Gnann et al. (2019) reported that using only the ϕ struggles to delineate baseflow variability in humid catchments, where the impact of soil water storage capacity (S_p) is as critical as that of the ϕ . Thus, Cheng et al. (2021) proposed an analytical curve for describing mean annual Q_b by introducing S_p as another theoretical boundary. Results show that the developed

84 curve agrees well with the observed *BFC* ($R^2 = 0.75$, RMSE = 0.058) and Q_b ($R^2 = 0.86$,
 85 RMSE = 0.19 mm), outperforming the original Budyko framework. Analogously, Yao et al.
 86 (2021) derived similar functions incorporated the ϕ , S_p and a shape parameter to model *BFC* and
 87 baseflow index (*BFI*, the ratio of Q_b to Q). These extended Budyko frameworks accounting for S_p
 88 have advantages in simulating Q_b . However, S_p is challenging to obtain through observations and
 89 often requires calibration (Cheng et al., 2021) or computation (Yao et al., 2021), adding certain
 90 uncertainties to the model. Notably, the calibration performance of Q_s in equation (1) to obtain W_p
 91 (the proxy of S_p) in the catchments of China are not always satisfactory, especially in the northern
 92 catchments (Figure S1). Moreover, the complicated forms can bring inherent uncertainties and
 93 these studies have not validated the formulations of Q_s , which are derived by subtracting Q_b from
 94 Q or fitting curves (Cheng et al., 2021; Neto et al., 2020), implying that they may overlook the
 95 physical processes represented by surface flow. In the subsequent discussion, the Budyko
 96 framework and extended Budyko equations are collectively referred to as the "Budyko-type
 97 formulations" (Table 1).

98 Many researchers have observed similar behavior of Q_b to Q (Cheng et al., 2021; Gnann et al.,
 99 2019; Wang and Wu, 2013). Is there a similar behavior for Q_s ? In a two-stage partitioning theory
 100 (L'vovich, 1979), runoff components are delineated based on the available water at each stage.
 101 Therefore, is there a general framework to unify different runoff components? Although various
 102 functional forms have been proposed for estimating runoff components in the literature, a
 103 universal method that reveals the mechanisms of mean annual runoff components generation and
 104 subsequent quantification and attribution is still in need.

105 **Table 1.** The Budyko-type formulations for estimating mean annual runoff components

References	Formulations	Parameters
Choudhury (1999); Yang et al. (2008)	$Q = P - \frac{P \times E_0}{(P^n + E_0^n)^{1/n}}$	n calibrated
Wang and Wu (2013)	$\frac{Q_b}{P} = 1 - \left[1 + \left(\frac{E_0}{P} \right)^{-v} \right]^{-1/v}$	v fitted
Neto et al. (2020)	$f_s(\phi) = \exp(-\phi^a + \delta_s^b)$ $f_B(\phi) = \exp(-\phi^c + \delta_B^d)$	a, b, c, d $\delta_s = \ln \left(\left[\frac{\bar{Q}_s}{\bar{P}} \right]_{max} \right)^{1/b}$

$$\delta_B = \ln \left(1 - \left[\frac{Q_S}{P} \right]_{max} \right)^{1/d}$$

fitted

$\frac{Q_s}{P} = -\frac{E_0 + S_p}{P} + \left[1 + \left(\frac{E_0 + S_p}{P} \right)^{\alpha_1} \right]^{1/\alpha_1}$	$\frac{Q_b}{P} = \frac{S_p}{P} + \left[1 + \left(\frac{E_0}{P} \right)^{\alpha_2} \right]^{1/\alpha_2}$	S_p, α_1, α_2
Cheng et al. (2021)	$- \left[1 + \left(\frac{E_0 + S_p}{P} \right)^{\alpha_2} \right]^{1/\alpha_2}$	calibrated
Q_b		
$= \frac{P + S_b - \sqrt{(P + S_b)^2 - 2aS_bP}}{a} \left[1 - \frac{1 + \frac{E_0}{P} \frac{P}{S_b} - \sqrt{\left(1 + \frac{E_0}{P} \frac{P}{S_b} \right)^2 - 2a \frac{E_0}{P} \frac{P}{S_b}}}{a} \right]$	S_b (estimated from cumulative distribution function), a (calibrated)	
Yao et al. (2021)	$Q = P - \frac{\frac{P}{S_b} + 1 - \sqrt{\left(\frac{P}{S_b} + 1 \right)^2 - 2a \frac{P}{S_b}}}{a} * \frac{E_0 + S_b - \sqrt{(E_0 + S_b)^2 - 2aE_0S_b}}{a}$	

106 Note that P is the mean annual precipitation, E_0 is the mean annual potential evapotranspiration, $f_S(\phi)$ and
107 $f_B(\phi)$ are the surface flow and baseflow function, respectively and S_p is the catchment storage capacity.

108 To address these questions, we derived a modified two-stage partitioning framework through
109 observational data analysis and theoretical derivation based on the Ponce-Shetty model (Ponce
110 and Shetty, 1995; Sivapalan et al., 2011) (namely the MPS model) at mean annual time scale. The
111 Ponce-Shetty model is a conceptual model with physical constraint developed at annual scale to
112 depict how precipitation is partitioned, stored and released in the catchment (Gnann et al., 2019).
113 It posits that annual precipitation is partitioned into Q_s and soil wetting (W) and, subsequently, the
114 resulting W is partitioned into Q_b and vaporization (V) (Sivapalan et al., 2011). The MPS model

115 enables large-sample catchments research, which may lead to new understanding of mean annual
116 water balance and allocation.

117 In general, the objectives of this study are to (1) develop a general and concise formulation to
118 describe runoff components variability at mean annual time scale; (2) validate and compare the
119 performance of the developed formulation against Budyko-type formulations; (3) attribute the
120 variations of runoff components induced by the changes of precipitation and other factors. Here,
121 we modify the Ponce-Shetty model according to some conditions and hypothesize a general
122 runoff components model (the MPS model), that describes Q_s , Q_b and Q as a function of
123 respective available water with one parameter. The MPS model is then validated over 662
124 catchments across China and the contiguous United States (the CONUS) over a wide range of
125 hydro-meteorological circumstances. The performance of the MPS model is also compared with
126 the Budyko-type formulations. Section 2 introduces the derivation of the MPS model. Section 3
127 provides the study catchments, data and the parameter estimation technique. Section 4 shows the
128 results followed by a discussion in Section 5. The conclusions are summarized in Section 6.

129 **2. Derivation of the Modified Ponce-Shetty Model**

130 L'vovich (1979) proposed a conceptual theory for the two-stage catchment water balance
131 partition at the annual time scale according to Horton's approach (Horton, 1933). Firstly,
132 precipitation is partitioned into surface flow (Q_s) and catchment wetting (W , stored water), and
133 then, the catchment wetting is partitioned into baseflow (Q_b) and vaporization (V , including
134 interception loss, evaporation and transpiration). Ponce and Shetty (1995) conceptualized the
135 partition of each step as the form of a competition, and derived the formulations of runoff
136 components based on the proportionality hypothesis. Sivapalan et al. (2011) reintroduced the
137 Ponce-Shetty equations as follows:

138 In the first stage, $P = Q_s + W$:

$$Q_s = \begin{cases} 0, & \text{if } P \leq \lambda_s W_p \\ \frac{(P - \lambda_s W_p)^2}{P + (1 - 2\lambda_s)W_p}, & \text{if } P > \lambda_s W_p \end{cases} \quad (1)$$

W

$$= \begin{cases} P, & \text{if } P \leq \lambda_s W_p \\ P - \frac{(P - \lambda_s W_p)^2}{P + (1 - 2\lambda_s)W_p}, & \text{if } P > \lambda_s W_p \end{cases} \quad (2)$$

$$P \rightarrow \infty, Q_s \rightarrow P - W_p, W \rightarrow W_p \quad (3)$$

139 In the second stage, $W = Q_b + V$:

Q_b

$$= \begin{cases} 0, & \text{if } W \leq \lambda_b V_p \\ \frac{(W - \lambda_b V_p)^2}{W + (1 - 2\lambda_b)V_p}, & \text{if } W > \lambda_b V_p \end{cases} \quad (4)$$

V

$$= \begin{cases} W, & \text{if } W \leq \lambda_b V_p \\ W - \frac{(W - \lambda_b V_p)^2}{W + (1 - 2\lambda_b)V_p}, & \text{if } W > \lambda_b V_p \end{cases} \quad (5)$$

$$W \rightarrow \infty, Q_b \rightarrow W - V_p, V \rightarrow V_p \quad (6)$$

140 where λ_s and λ_b are the surface flow and baseflow initial abstraction coefficients, respectively,
141 which range from 0 to 1. The larger value of λ , the more difficult it is to generate flow. W_p and V_p
142 are catchment wetting potential and vaporization potential, respectively, which are greater than 0.
143 The relative $\lambda_s W_p$ and $\lambda_b V_p$ are the surface flow and baseflow generation thresholds,
144 respectively.

145 Note that the interannual water storage change is supposed to be negligible (Ponce and Shetty,
146 1995). In a companion paper of Sivapalan et al. (2011), Harman et al. (2011) employed the
147 annual Ponce-Shetty model at mean annual time scale and validated its applicability. Using the
148 first phase as an example, Q_s can be considered a function of λ_s , denoted as $f(\lambda_s)$:

$f(\lambda_s)$

$$= \begin{cases} 0, & \text{if } \lambda_s \geq P/W_p \\ \frac{(P - \lambda_s W_p)^2}{P + (1 - 2\lambda_s)W_p}, & \text{if } \lambda_s < P/W_p \end{cases} \quad (7)$$

149 When $\lambda_s < P/W_p$, the Taylor expansion of $f(\lambda_s)$ at $\lambda_s=0$ is:

$$f(\lambda_s) = f(0) + f'(0) * \lambda_s + \frac{f''(0)}{2!} * \lambda_s^2 + \dots + \frac{f^n(0)}{n!} * \lambda_s^n + \dots \quad (8)$$

150 Hence, we have the zeroth-order approximation:

$$f(\lambda_s) \approx \frac{P^2}{P + W_p} \quad (9)$$

151 When the remainder term is relatively small, an approximation equation can be used to
152 estimate the multi-year Q_s as:

$$Q_s = \frac{P^2}{P + W_p} \quad (10)$$

153 In addition, the zeroth-order approximation of Q_b can be similarly obtained as:

$$Q_b = \frac{W^2}{W + V_p} \quad (11)$$

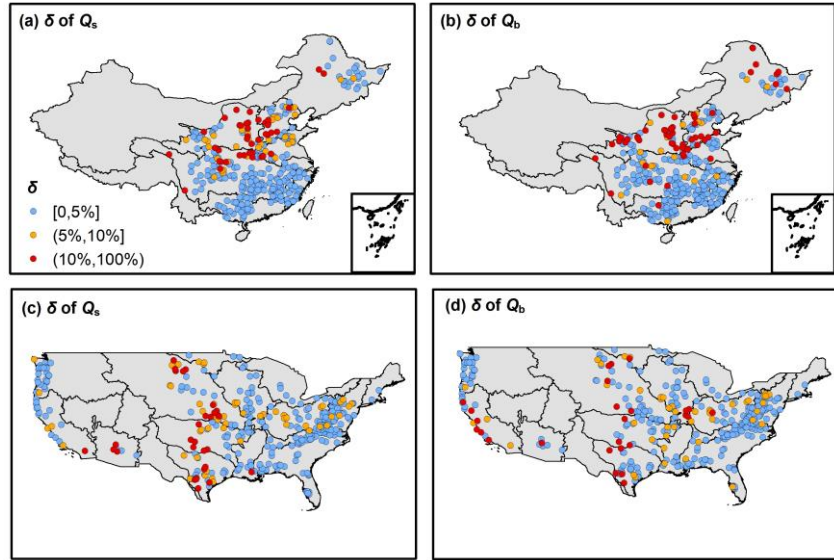
154 To evaluate the impact of the remainder term, we calculate the relative bias (δ) of runoff
155 components for 312 basins in China and 350 basins in the United States using the approximate
156 equations (Eq (10) and Eq (11)) and the original Ponce-Shetty equations (Eq (1) and Eq (4)) (data
157 sources in Section 3.1). The parameters in the original Ponce-Shetty equations are calibrated
158 using the nonlinear least squares method. The δ is calculated as:

$$\delta = \frac{|\tilde{Q}_y - Q_y|}{Q_y} \quad (12)$$

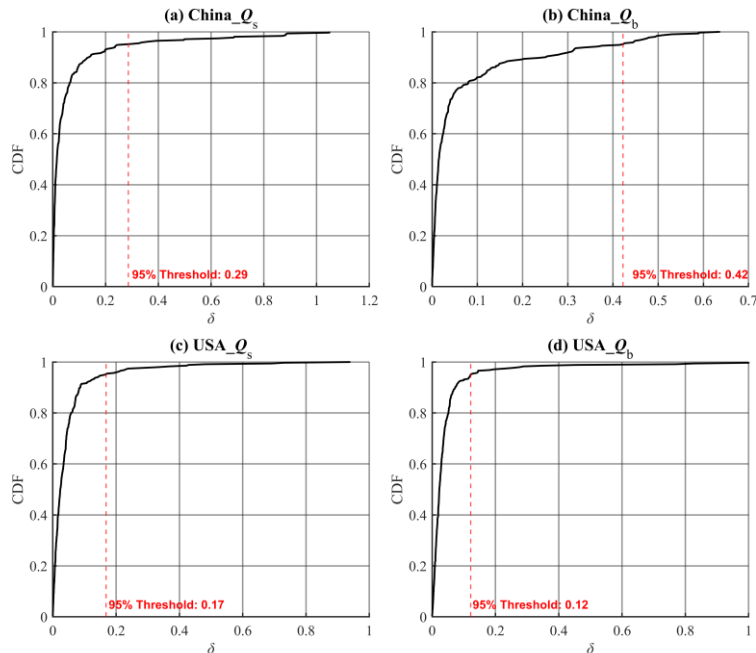
159 where Q_y represents runoff components estimated by the Ponce-Shetty equations, and \tilde{Q}_y
160 represents runoff components estimated by the approximate equations (Eq (10) and Eq (11)).

161 The spatial distribution of δ and the cumulative distribution functions (CDFs) of δ are
162 shown in Figure 1 and Figure 2, respectively. As shown in Figure 1, 77% of the basins have an δ
163 of less than 5%. The average δ for estimating Q_s is 6.5% in China and 4.8% in the United States,
164 while the average δ for estimating Q_b is 7.9% in China and 6.6% in the United States, with
165 larger deviations observed in arid basins. Figure 2 indicate that the δ values for the approximate
166 model are within acceptable limits across both China and CONUS. The relatively low 95%
167 threshold values, particularly for the USA datasets, suggest that the majority of predictions fall
168 within a narrow error range, indicating robust model performance. This acceptability of δ across
169 regions and variables highlights the approximate equations' capability to maintain prediction

170 accuracy under varying geographical and hydrological conditions, indicating that the Zeroth-order
 171 approximation is representative for the original Ponce-Shetty model.



172
 173 **Figure 1.** The distribution of relative bias (δ) between the results by the approximate equations
 174 (Eq (10) and Eq (11)) versus the original Ponce-Shetty equations (Eq (1) and Eq (4)). The first
 175 row shows the results for 312 basins in China, and the second row shows the results for 350
 176 basins in CONUS. The first column corresponds to surface flow (Q_s), and the second column
 177 corresponds to baseflow (Q_b).



178
 179 **Figure 2.** Cumulative distribution functions (CDFs) of the relative bias (δ) for each dataset,
 180 represented by four subplots corresponding to different regions and variables: (a) China_ Q_s , (b)

181 China_ Q_b , (c) USA_ Q_s , and (d) USA_ Q_b . Each subplot includes a red dashed line indicating the
182 95% δ threshold

183 Therefore, we can approximately consider that on a multi-year scale, Q_s and Q_b can be
184 estimated using the zeroth-order approximation in Eq (10) and Eq (11). We subsequently assume
185 a similar formulation of mean annual Q :

$$Q = \frac{P^2}{P + U_p} \quad (13)$$

186 where U_p is the parameter representing the upper limit of the portion remaining after precipitation
187 is allocated to runoff, hereafter we refer to U_p as evapotranspiration potential.

188 Integrating equations (10), (11) and (13), we conclude a general formulation to depict
189 multi-year variability of runoff components and their quantification, hereafter referred to as the
190 modified Ponce-Shetty model (the MPS model):

$$Q_y = \frac{X^2}{X + M} \quad (14)$$

191 where Q_y represents runoff components (i.e., Q , Q_s , Q_b), X corresponds to the available water of
192 each runoff component, i.e., P is the available water of Q and Q_s , and W the available water of Q_b .
193 M is an integrated parameter, representing the comprehensive effects of catchment characteristics
194 and atmospheric water and energy demand.

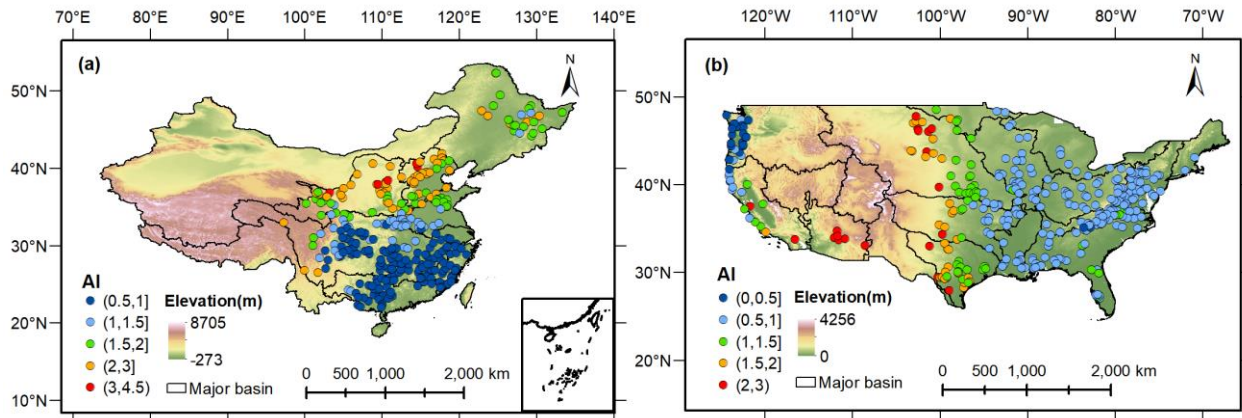
195 The MPS model encodes runoff components as a function of available water with only one
196 parameter, which not only considers processes of runoff generation with physical constraints, but
197 also, compared to the Budyko-type formulations and the original Ponce-Shetty model, is more
198 concise in form and requires fewer parameters. Therefore, it is possible to estimate the long-term
199 runoff components when only long-term variables are known.

200 3. Data and Methodology

201 3.1. Data

202 To validate the reliability of the MPS model, daily hydrological and meteorological data from
203 312 catchments in China (Li et al., 2024) and 350 catchments in the CONUS are collected. The

204 criteria for catchments screening can refer to He et al. (2025). The location of all the catchments
 205 hydrological stations is shown in Figure 3.



206
 207 **Figure 3.** Location of hydrological stations for the (a) 312 catchments in China and (b) 350
 208 catchments in the CONUS, colored by the value of aridity index (ϕ , namely E_0/P).

209 In China, precipitation data at 0.25° spatial resolution are obtained from the China
 210 Gauge-based Daily Precipitation Analysis (CGDPA) (Shen and Xiong, 2016). Other
 211 meteorological data, including wind speed, sunshine hours, relative humidity, and air temperature,
 212 are from about 736 stations of the China Meteorological Data Service Center
 213 (<http://data.cma.cn/en>, last access: 11 November 2023). The in-site meteorological data are
 214 interpolated into a 10-km grid using the inverse-distance weighted method (Yang et al., 2014).
 215 We use the Penman equation (Penman, 1948) to estimate E_0 of each grid using standard
 216 meteorological inputs (e.g., radiation, humidity, wind, temperature). The Penman equation is
 217 widely recommended to estimate E_0 at catchment scale due to its physical basis (Pimentel et al.,
 218 2023; Wang et al., 2025), and it provides a consistent reference for our annual, large-sample
 219 analyses. The aridity index ϕ is subsequently calculated as E_0/P . All grid data are aggregated
 220 and lumped for individual catchments. The discharge data are collected from the Hydrological
 221 Bureau of the Ministry of Water Resources of China (<https://www.mwr.gov.cn/english/>, last
 222 access: 20 December 2023) and are selected based on the length of records exceeding 35 years
 223 with less than 5% missing data. The time range for all data is 1960-2000.

224 In the CONUS, we use data set from CAMELS (Addor et al., 2017; Newman et al., 2015). The
 225 CAMELS data set provides 662 catchments with daily time series of precipitation and observed
 226 runoff along with aridity index, and most catchments contain 35 years of continuous runoff from

227 1980 to 2014. The criteria for excluding catchments are referred to Gnann et al. (2019), and
228 finally 350 catchments remained.

229 We use the one-parameter Lyne-Hollick digital filter (Lyne, 1979) to separate daily Q_s and Q_b
230 from daily Q . The Lyne-Hollick method is applied forward, backward, and forward again with a
231 filter parameter of 0.925 and has manifested to be reliable to obtain runoff components (Lee and
232 Ajami, 2023). We use the separated Q_s and Q_b as the reference. Although there are other baseflow
233 separation algorithms, according to Troch et al. (2009), the choice of baseflow separation
234 algorithm is not a significant determinant of the water balance at the annual scale.

235 All the hydrological and meteorological data are aggregated to the annual and mean annual
236 time scales for further analysis.

237 **3.2. Calibration and Validation**

238 Spatially, to verify the MPS model's ability to characterize the variability of runoff components
239 between catchments, we utilize the least squares fitting algorithm to estimate parameters, i.e., W_p ,
240 V_p and U_p . The three parameters are restricted to being between 0 mm and 50, 000 mm, which is
241 considered high enough to not affect the parameter estimation (Gnann et al., 2019).

242 In terms of time, we split all data into two periods for parameter calibration and validation of
243 Eq. (14) for individual catchments. In China, the data ranges from 1960 to 2000, so we use the
244 first 31 years (1960-1990) as the calibration period and the remaining 5-10 years (1991-2000) as
245 the validation period. In the CONUS, the calibration period is chosen as 1980-2000, and the
246 validation period is from 2001 to 2014. When we know mean annual Q_s , Q_b , Q , P and W of the
247 first period, the parameters, i.e., W_p , V_p and U_p , can be derived from Eq. (14). Postulating the
248 parameters remain unchanged during two periods, we consequently can estimate the mean annual
249 Q_s , Q_b and Q of the second period using Eq. (14). Note that the catchment wetting W is calculated
250 as the difference of the P and estimated Q_s .

251 The surface flow fraction (*SFC*, the ratio of surface flow to precipitation) and baseflow fraction
252 (*BFC*, the ratio between baseflow and precipitation) represent the proportion of rainfall becoming
253 different runoff components, which are commonly used to quantify surface flow and baseflow
254 (Wang and Wu, 2013). Therefore, we evaluate the simulation of *SFC* and *BFC* as well as the
255 volume of runoff components.

256 The performance of the MPS model is evaluated by the coefficient of determination (R^2) and
 257 the root mean square error (RMSE):

$$R^2 = \left(\frac{\sum_{i=1}^N (X_{sim,i} - \bar{X}_{sim})(X_{obs,i} - \bar{X}_{obs})}{\sqrt{\sum_{i=1}^N (X_{sim,i} - \bar{X}_{sim})^2 \sum_{i=1}^N (X_{obs,i} - \bar{X}_{obs})^2}} \right)^2 \quad (15)$$

$$RMSE = \sqrt{\frac{1}{N} \sum_{i=1}^N (X_{sim,i} - X_{obs,i})^2} \quad (16)$$

258 where X represents the evaluated variable, i.e., mean annual Q , Q_s and Q_b , SFC and BFC in this
 259 study. The subscript *obs* and *sim* represents the observed and simulated value, respectively.
 260 Higher R^2 and lower RMSE indicate good model performance.

261 3.3. Attribution analysis

262 We split the data into the first period (1960-1990 in China and 1980-2000 in the CONUS) and
 263 the second period (1991-2000 in China and 2001-2014 in the CONUS) to attribute runoff
 264 components variation between two periods. Note that the attribution of ΔQ is only conducted in
 265 China because the E_0 in CAMELS dataset is a constant in each catchment. In the MPS model, we
 266 consider that the runoff changes between two long-term periods are caused by available water and
 267 other environmental and anthropogenic factors (such as land cover/use change and
 268 evapotranspiration variation) encoded by parameters. For the changes of surface flow (ΔQ_s) and
 269 total runoff (ΔQ), postulating that each variable is independent in the MPS model, the first-order
 270 approximation of the ΔQ_s and ΔQ from the second period to the first period can be expressed as
 271 (Milly and Dunne, 2002):

$$\Delta Q_s = \frac{\partial Q_s}{\partial P} \Delta P + \frac{\partial Q_s}{\partial W_p} \Delta W_p \quad (17a)$$

$$\Delta Q = \frac{\partial Q}{\partial P} \Delta P + \frac{\partial Q}{\partial U_p} \Delta U_p \quad (17b)$$

272 where the two terms on the right side of equation (17a) respectively represent changes in Q_s
 273 caused by changes in P (ΔQ_{s-P}) and other factors (ΔQ_{s-W_p}), and the two terms on the right side
 274 of equation (17b) respectively represent changes in Q caused by changes in P (ΔQ_P) and other
 275 factors (ΔQ_{U_p}). For convenience, we refer partial derivative coefficient $\frac{\partial Q_s}{\partial P}$, $\frac{\partial Q_s}{\partial W_p}$, $\frac{\partial Q}{\partial P}$ and $\frac{\partial Q}{\partial U_p}$ in

276 equation (17) as ζ_{Qs-P} , ζ_{Qs-Wp} , ζ_{Q-P} and ζ_{Q-Wp} , which can be calculated as:

$$\zeta_{Qs-P} = \frac{P^2 + 2PW_p}{(P + W_p)^2} \quad (18a)$$

$$\zeta_{Qs-Wp} = \frac{-P^2}{(P + W_p)^2} \quad (18b)$$

$$\zeta_{Q-P} = \frac{P^2 + 2PU_p}{(P + U_p)^2} \quad (18c)$$

$$\zeta_{Q-Wp} = \frac{-P^2}{(P + U_p)^2} \quad (18d)$$

277 The changes of baseflow (ΔQ_b) is induced by the variations of the W and V_p . However, we
 278 focus more on the impact of P in application. Therefore, we combine equation (10), (11) and $W =$
 279 $P - Q_s$, so the Q_b can be calculated as :

$$Q_b = \frac{P^2 W_p^2}{(P + W_p)(PW_p + PV_p + W_p V_p)} \quad (19)$$

280 The ΔQ_b can be attributed as the variations of P , W_p and V_p :

$$\Delta Q_b = \frac{\partial Q_b}{\partial P} \Delta P + \frac{\partial Q_b}{\partial W_p} \Delta W_p + \frac{\partial Q_b}{\partial V_p} \Delta V_p \quad (20)$$

281 where the three terms on the right side of equation (20) respectively represent changes in Q_b
 282 caused by changes in P (ΔQ_{b-P}), W_p (ΔQ_{b-Wp}) and V_p (ΔQ_{b-Vp}). The partial derivative
 283 coefficient $\frac{\partial Q_b}{\partial P}$ (ζ_{Qb-P}), $\frac{\partial Q_b}{\partial W_p}$ (ζ_{Qb-Wp}) and $\frac{\partial Q_b}{\partial V_p}$ (ζ_{Qb-Vp}) can be calculated as:

$$\zeta_{Qb-P} = \frac{2P^2 W_p^3 V_p + P^2 W_p^4 + 2P W_p^4 V_p}{(P + W_p)^2 (PW_p + PV_p + W_p V_p)^2} \quad (21a)$$

$$\zeta_{Qb-Wp} = \frac{P^4 W_p^2 + 2P^4 W_p V_p + 2P^3 W_p^2 V_p}{(P + W_p)^2 (PW_p + PV_p + W_p V_p)^2} \quad (21b)$$

$$\zeta_{Qb-Vp} = \frac{-P^2 W_p^2}{(P + W_p)^2 (PW_p + PV_p + W_p V_p)^2} \quad (21c)$$

284 To verify the applicability of the MPS model for runoff components attribution, we compare
 285 the calculated ΔQ_s , ΔQ_b and ΔQ using equation (17) and (20) with the observed ΔQ_s , ΔQ_b
 286 and ΔQ between two periods. The evaluation metrics are R^2 and RMSE.

287 The relative contribution ratios of P and other factors to runoff components change are
 288 calculated as:

$$\eta_P = \frac{|\Delta Q_{y-P}|}{|\Delta Q_{y-P}| + |\Delta Q_{y-Wp}| + |\Delta Q_{y-Vp}|} \times 100\% \quad (22a)$$

$$\eta_{Wp} = \frac{|\Delta Q_{y-Wp}|}{|\Delta Q_{y-P}| + |\Delta Q_{y-Wp}| + |\Delta Q_{y-Vp}|} \times 100\% \quad (22b)$$

$$\eta_{Vp} = \frac{|\Delta Q_{y-Vp}|}{|\Delta Q_{y-P}| + |\Delta Q_{y-Wp}| + |\Delta Q_{y-Vp}|} \times 100\% \quad (22c)$$

289 where η_P , η_{Wp} and η_{Vp} are the relative contribution ratios of P , W_p and V_p to runoff
 290 components, respectively. We subsequently use the absolute values of η to identify the dominant
 291 factor impacting runoff components.

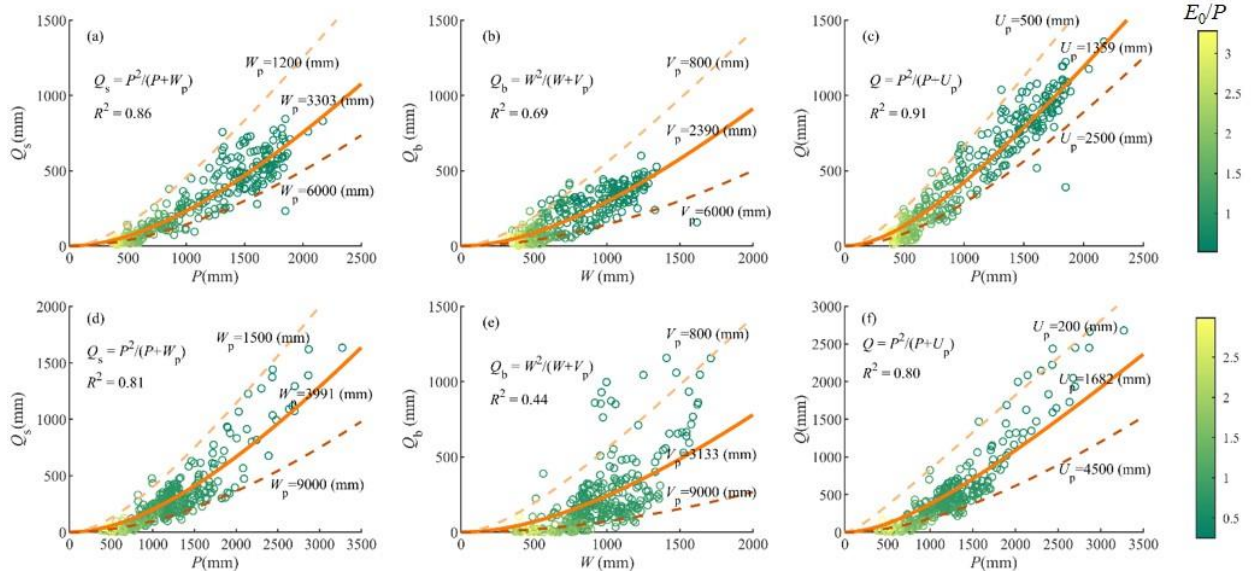
292 4. Results

293 4.1. Inter-Catchment Variability of Runoff Components

294 We employ the MPS model to fit the relationship between mean annual available water and
 295 runoff components. In China, as shown in Figure 4(a-c), the MPS model performs well in
 296 describing runoff components variability between catchments, with R^2 values of 0.86, 0.68 and
 297 0.91 for fitting Q_s , Q_b and Q , respectively. The solid lines are the best-fitted MPS curves derived
 298 using the least squares fitting algorithm, implying the median values of different parameters. We
 299 also give the potential upper and lower limits of W_p , V_p and U_p across catchments. Similarly,
 300 Figure 4(d-f) illustrates that the MPS model achieves good fitting in the CONUS, with R^2 of 0.81,
 301 0.44 and 0.80 for fitting Q_s , Q_b and Q , respectively. The fitted parameters in the CONUS are
 302 smaller than those in China, while they have more comprehensive ranges between catchments,
 303 meaning a more significant heterogeneity in climate and underlying surface.

304 Figures 4 demonstrates that the MPS model can effectively reproduce the spatial variability of
 305 different runoff components along with the aridity index (E_0/P), which are primarily controlled by
 306 the available water of the corresponding partition stage. The performance of MPS model to fit Q_s
 307 and Q is better than that of Q_b , indicating that the factors controlling Q_b are more complicated and

308 not fully reflected in the model. With catchment properties and other factors (integrated by the
 309 parameters in the MPS model) remaining unchanged, the more the available water, the higher the
 310 runoff generated. Conversely, smaller parameter values are associated with greater runoff for a
 311 given amount of available water.



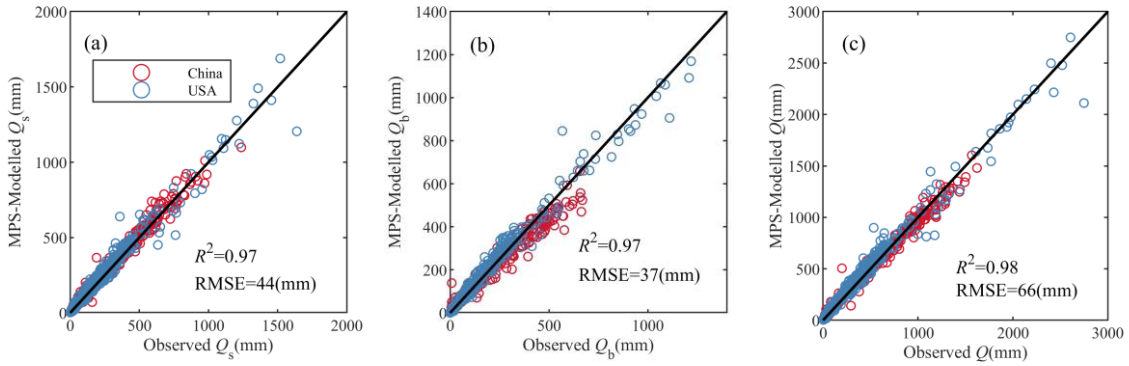
312
 313 **Figure 4.** The MPS model relating (a) P versus Q_s , (b) W versus Q_b and (c) P versus Q in China
 314 and (d) P versus Q_s , (e) W versus Q_b and (f) P versus Q in the CONUS. The lines are the fitted
 315 MPS curves with best fitting (solid line) and potential upper limit and lower limit (dashed lines)
 316 parameters.

317 4.2. Validation of Runoff Components Estimation

318 Figure 5 shows the estimated mean annual Q_s , Q_b and Q in validation periods using the MPS
 319 model with inverted parameters in equation (14) in China and the CONUS. The simulated runoff
 320 components match very well with the observed, with R^2 greater than 0.97 and RMSE less than 66
 321 mm. There is no significant difference in the performance in simulating Q_s , Q_b , and Q , except for
 322 a slight underestimation in simulating Q_b of catchments in China and some in the CONUS.

323 In panels (a), (b), and (c), we observe that the scatter points for both China (red circles) and the
 324 CONUS (blue circles) are closely aligned with the 1:1 line, further underscoring the strong
 325 correlation between modeled and observed values. Specifically, the results show that the MPS
 326 model effectively captures surface flow (Q_s), baseflow (Q_b), and total runoff (Q) for both regions.
 327 Despite the generally good performance, a slight underestimation of Q_b is evident in a subset of
 328 catchments in China and, to a lesser extent, in the CONUS. However, these discrepancies are

329 minimal and do not significantly detract from the model's overall accuracy.

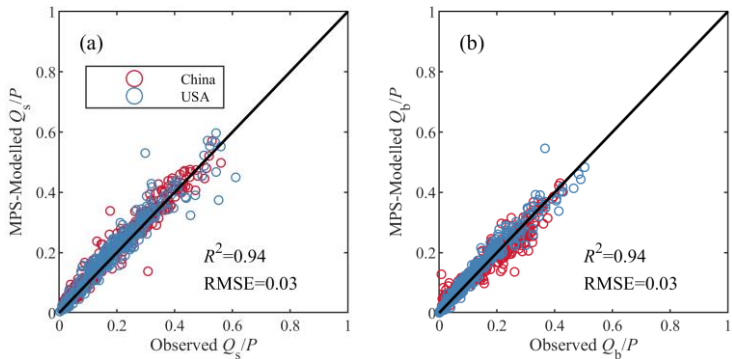


330

331 **Figure 5.** The observed and simulated mean annual (a) surface flow, (b) baseflow and (c) total
332 runoff by the MPS model in China (red circles) and the CONUS (blue circles).

333 Figure 6 presents the estimation of *SFC* and *BFC* in validation periods using the MPS model.
334 Similar to the simulation of Q_s , the two methods also show highly consistent estimation of *SFC*
335 (panel (a)), with R^2 of 0.94 and RMSE of 0.03. This demonstrates the MPS model's robust
336 capability to estimate the surface flow fraction in China and the CONUS, closely aligning with
337 the observed data. Panel (b) presents the estimation of *BFC*, where the MPS model achieves
338 significant accuracy, reflected by the same R^2 and RMSE values (0.94 and 0.03, respectively).
339 This strong performance indicates that the MPS model is highly effective in simulating *SFC* and
340 *BFC* across various catchments.

341



342

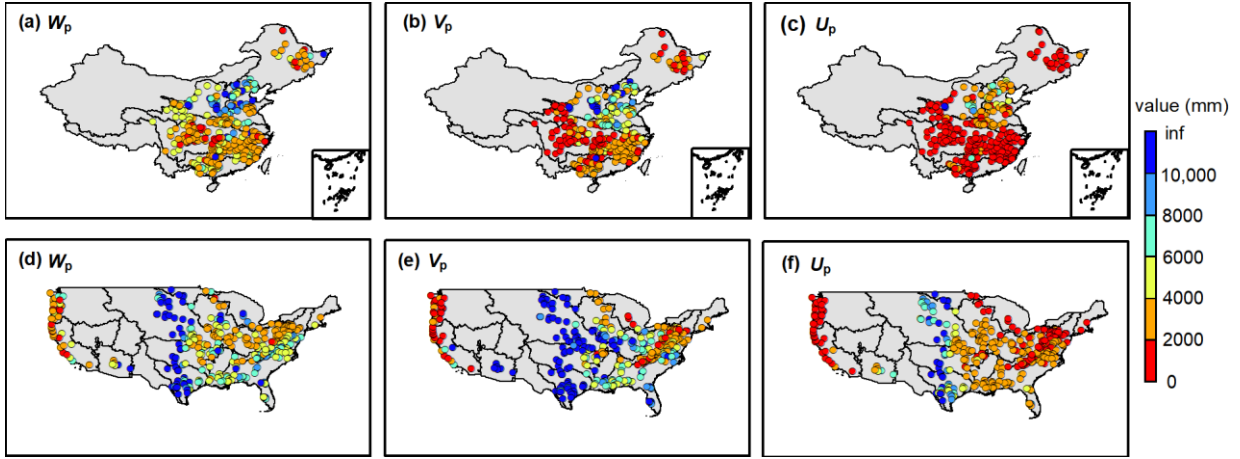
343 **Figure 6.** The observed and simulated (a) surface flow fraction (Q_s/P) and (b) baseflow fraction
344 (Q_b/P) by the MPS model in China (red circles) and the CONUS (blue circles).

345 Figure 5 and Figure 6 document that the MPS model can effectively estimate the multi-year
346 average of all runoff components and the proportions of precipitation allocated to runoff.

347 The good validation performance of the MPS model verified our hypothesis that the parameters

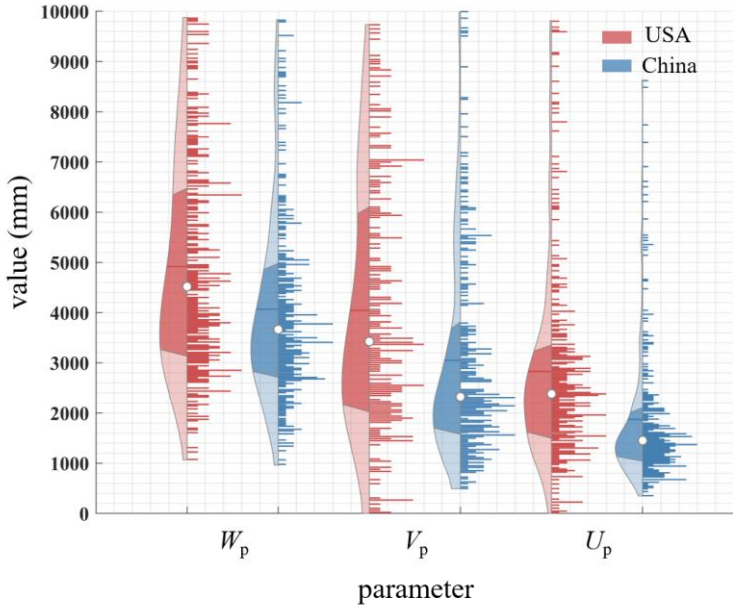
347 in the general formulations remain stable at the mean annual time scale. The parameters reflect
348 the comprehensive impact of climate and catchment characteristics, i.e., catchment wetting
349 potential (W_p), vaporization potential (V_p) and the upper limit of the portion remaining after
350 precipitation is allocated to runoff (U_p). As shown in Figure 7(a-c), the spatial distribution of the
351 parameters across China exhibits pronounced divergence between the northern and southern
352 catchments, as well as the eastern and the western. The W_p , V_p and U_p exhibit similar spatial
353 patterns, which can be approximately divided into two tiers from north to south. In the catchments
354 of the Songliao River Basin in the northeast, the Yangtze River Basin and Pearl River Basins in
355 the south, the parameters are relatively small, with W_p and U_p ranging from 0 to 2000 mm, and V_p
356 from 0 to 4000 mm, resulting large flow. In the catchments of the Yellow River Basin, Huaihe
357 River Basin and Haihe River Basin in the north, the parameters are quite large and usually more
358 than 5000 mm and even 8000 mm, leading to small flow. From west to east, W_p exhibits higher
359 values in the Yangtze and Yellow Rivers Basin sources, whereas V_p and U_p are smaller in the
360 source regions. This disparity may reflect variations in the two-stage partition of precipitation,
361 contributing to spatial differences in total runoff. According to Figure 7(c), we can deduce that
362 the spatial distribution of higher total runoff in south and lower in north across China, aligning
363 with previous observational studies (He et al., 2021; He et al., 2022; Yang et al., 2019).

364 Figure 7(d-f) shows an evident west-east discrepancy of the three parameters across the
365 CONUS. Typically, W_p , V_p and U_p of the catchments in the west coast and eastern regions are less
366 than 5000 mm, while parameters in the central United States are extensive with values more than
367 8000 mm. This indicates relatively low flow in the central regions. Notably, the parameters upper
368 limits in the catchments of the CONUS are significantly higher than those in China. The
369 extremely large values may be associated with significant parameter uncertainty (Gnann et al.,
370 2019). Figure 7 demonstrates that the values of the three parameters are larger in arid catchments
371 and their spatial patterns are similar to that of climate zoning, which provides insights for
372 parameterization.



373
374 **Figure 7.** The (a) wetting potential (W_p), (b) vaporization potential (V_p) and (c)
375 evapotranspiration potential (U_p) of the catchments in China and (d) wetting potential (W_p), (e)
376 vaporization potential (V_p) and (f) evapotranspiration potential (U_p) of the catchments in the
377 CONUS.

378 Figure 8 shows the violin plots of the parameters in the catchments of China and the CONUS.
379 The median values of W_p , V_p , and U_p in China are 3659 mm, 2220 mm and 1453 mm,
380 respectively. The median values of W_p , V_p , and U_p in the CONUS are 4531 mm, 3424 mm and
381 2385 mm, respectively. Overall parameters in China are smaller and denser than those in the
382 CONUS, implying a smaller variability of runoff components in China. Furthermore, the C_v value
383 of V_p (1.6 in China and 6.8 in the CONUS) is the largest, followed by U_p (0.9 in China and 1.6 in
384 the CONUS), and the smallest for W_p (0.6 in China and 1.5 in the CONUS). This indicates that
385 the parameter dispersion controlling the second partition stage of rainfall is the greatest, which
386 could partly account for the challenges in accurately estimating Q_b .

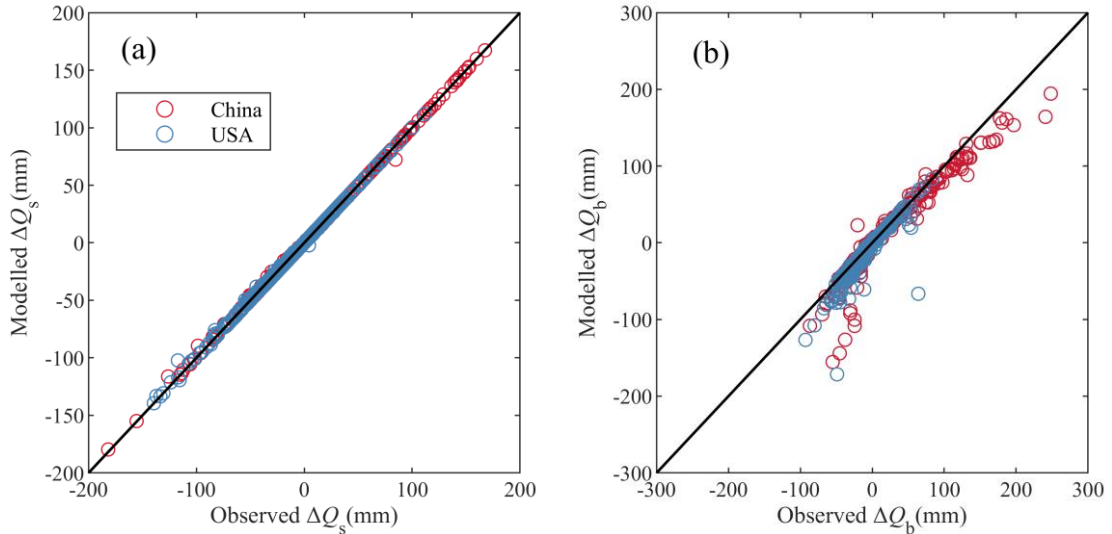


387

388 **Figure 8.** Violin plots of the parameters in the catchments of China and the CONUS. In each
 389 violin plot, the left side represents the distribution, with the shaded area indicating the box plot,
 390 the dot representing the mean, and the right side showing the histogram. The length of the
 391 histogram represents the number of catchments (values larger than 10,000 are not shown).

392 4.3. The Changes Attribution of Runoff Components

393 The metrics to evaluate the attribution results between the changes of the observed and
 394 simulated runoff components are shown in Table 2. We use the MPS model to estimate the
 395 changes of Q_s (ΔQ_s), Q_b (ΔQ_b) and Q (ΔQ) from two long-term periods by equation (17) and
 396 (20), and for comparison, we use the Budyko framework to estimate ΔQ , which is considered as
 397 the changes induced by P , E_0 , and parameter n (the calculation formulations can refer Zhang et al.
 398 (2018)). The estimated and observed runoff components variations exhibit high consistency
 399 (Figure 9), with an R^2 of 0.99 and RMSE of 1.6 mm of ΔQ_s attribution and R^2 of 0.88 and RMSE
 400 of 18 mm of ΔQ_b attribution, respectively. As for ΔQ , both the MPS model and the Budyko
 401 framework can attain satisfactory performance, while the MPS model has a higher R^2 (0.91) than
 402 the Budyko framework (0.89). Table 2 demonstrates that the MPS model can accurately quantify
 403 changes in runoff components over two periods. Subsequently, we quantify the contribution of
 404 precipitation and other factors (encoded by parameter W_p and V_p) to ΔQ_s and ΔQ_b .



405

406 **Figure 9.** The observed and modelled (a) surface flow and (b) baseflow by the MPS model.

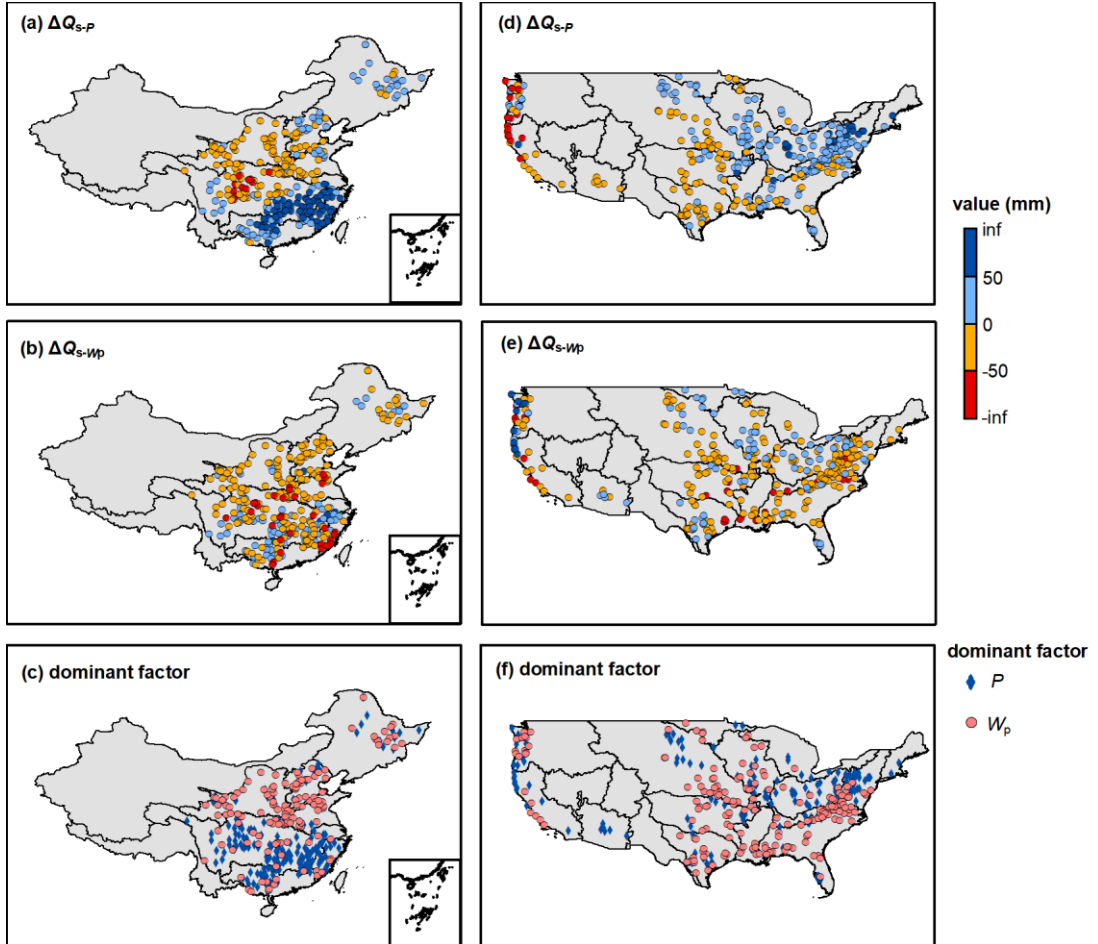
407

Table 2. The metrics of the attribution validation

Variables	R^2	RMSE (mm)
ΔQ_s	0.99	1.6
ΔQ_b	0.90	16
ΔQ (the MPS model)	0.91	42
ΔQ (the Budyko framework)	0.89	41

408 Figure 10 shows the ΔQ_s induced by P (ΔQ_{s-P}) and other factors (ΔQ_{s-W_p}) along with the
 409 dominant factor in the catchments of China and the CONUS. From 1960-1990 to 1991-2000 in
 410 China, the multi-year variation in P has resulted in Q_s change ranging from -105 to 344 mm,
 411 mainly increasing Q_s in the catchments of the Songliao River Basin, the middle and lower
 412 Yangtze River Basin, the Southeast River Basin and Pearl River Basin, and decreasing Q_s in the
 413 catchments of the Yellow River Basin and the upper Yangtze River Basin (Figure 10(a)). The
 414 variations of other factors, such as land use/cover change and human activities, have resulted in
 415 Q_s change ranging from -186 to 124 mm, primarily decreases Q_s in 70% catchments (Figure
 416 10(b)). P and other W_p are the dominant factor altering Q_s in southern and northern China,
 417 respectively (Figure 10(c)). From 1980-2000 to 2000-2014 in the CONUS, variation in P has
 418 resulted in Q_s change ranging from -469 to 149 mm, mainly increasing Q_s in the catchments of
 419 Interior Plains (except Great Plains), Coastal Plain, Interior highlands and Appalachian Plain, and
 420 decreasing Q_s in the catchments of the Great Plains and Pacific Mountains (the physiographic

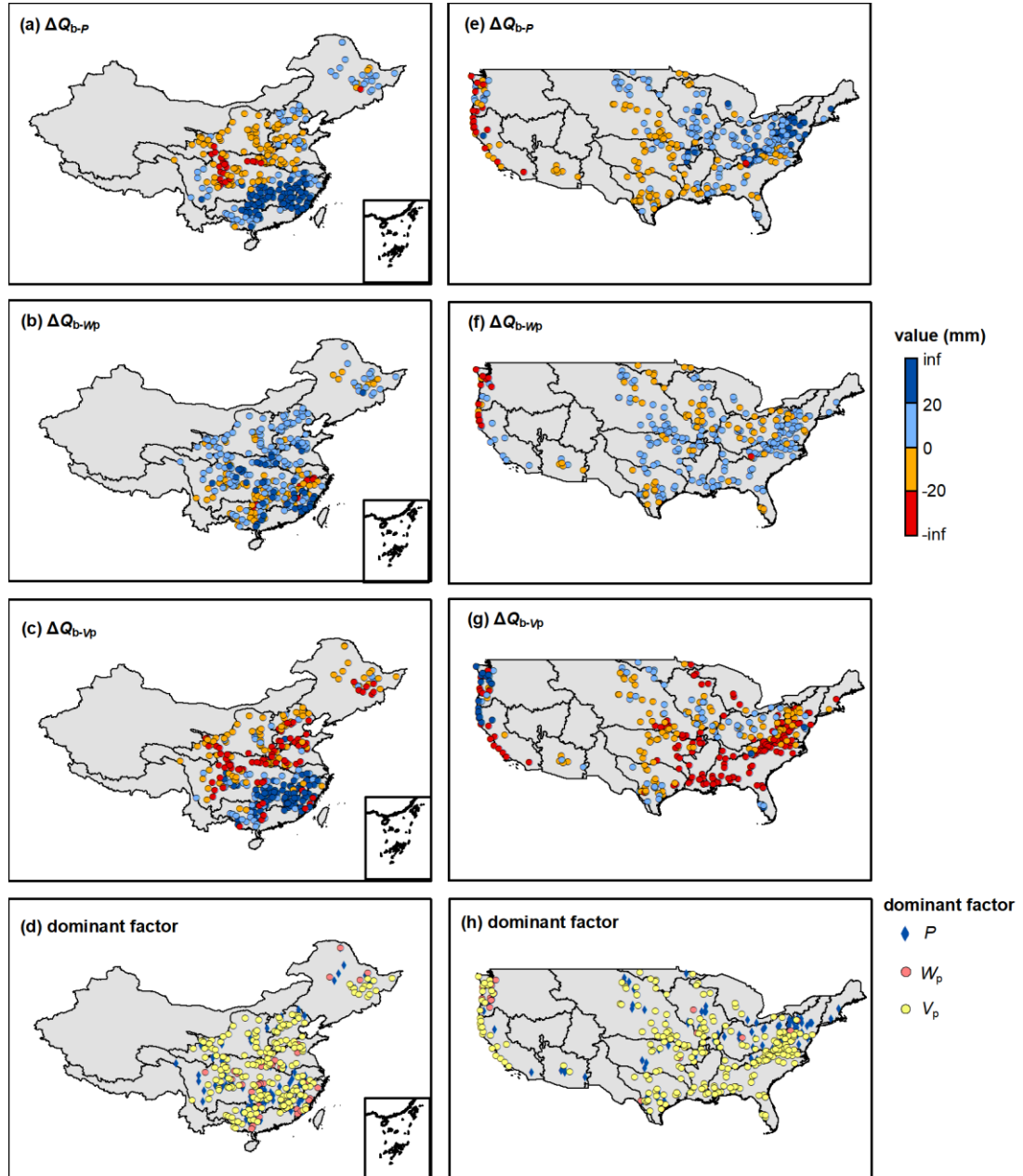
421 divisions are referred to Wu et al. (2021)) (Figure 10(d)). The variations of other factors have
 422 resulted in Q_s change ranging from -230 to 467 mm, primarily decreases Q_s in 75% catchments
 423 (Figure 10(e)). The catchments in the CONUS dominated by P and W_p account for 43% and 57%,
 424 respectively (Figure 10(f)).



425
 426 **Figure 10.** The surface flow change induced by precipitation and wetting potential (W_p) along
 427 with the dominant controlling factor.

428 Figure 11 shows the ΔQ_b induced by P (ΔQ_{b-P}), W_p (ΔQ_{b-Wp}) and V_p (ΔQ_{b-Vp}) in the
 429 catchments of China and the CONUS. The spatial pattern of the effect of P on Q_b is similar to that
 430 of the Q_s , resulting in Q_b change from -38 to 79 mm in China (Figure 11(a)) and -129 to 92 mm in
 431 the CONUS (Figure 11(e)), respectively. Catchment wetting potential has a positive effect on Q_b
 432 in 70% and 75% catchments of China and the CONUS, respectively (Figure 11(b)and (f)), mainly
 433 in the northern China and the Interior Highlands, Coastal Plain and Appalachian Highlands of the
 434 CONUS. Vaporization potential has a negative effect on Q_b in 56% and 77% catchments of China
 435 and the CONUS, respectively, mainly in the upper Yangze River Basin and northern China and

436 the central and southeastern CONUS (Figure 11(c)and (g)). Although V_p is the dominant factor
 437 controlling Q_b variation in most catchments in both China (62%) and the CONUS (71%) (Figure
 438 11(d)and (h)), the contributions of the P , W_p and V_p are not significantly discrepant in terms of
 439 magnitude.



440

441 **Figure 11.** The baseflow change induced by precipitation, wetting potential (W_p) and
 442 vaporization potential (V_p) along with the dominant controlling factor.

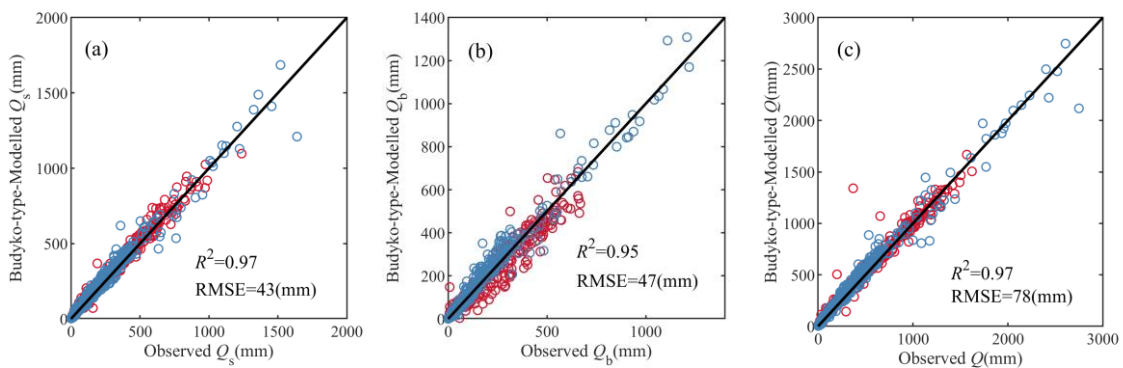
443 Overall, Figure 10 and 11 illustrate that the variation of Q_s is jointly controlled by P and other
 444 factors, while the variation of Q_b is mainly influenced by V_p . This demonstrates that Q_s is closely
 445 related to rainfall and soil storage capacity, while Q_b is more affected by catchment attributes,

446 atmospheric water and energy demand, etc. In regions where runoff components are reduced,
 447 focus should be given to the risks of drought and river discontinuity; conversely, in areas
 448 experiencing runoff components increase, there is a need to guard against the risk of flooding.

449 **5. Discussion**

450 **5.1. Superiorities of the MPS Model**

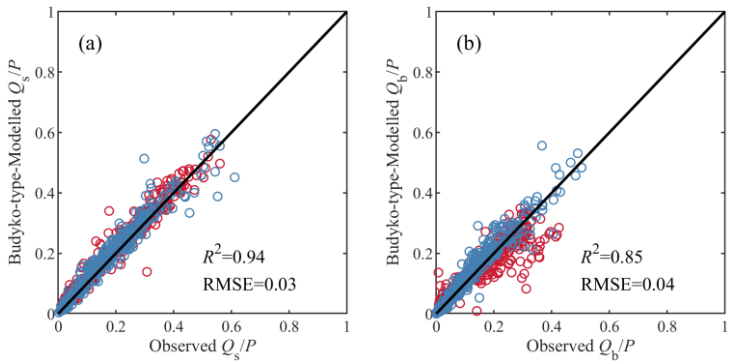
451 The researches about long-term runoff components quantification and attribution are currently
 452 fragmented and region-specific (Beck et al., 2013; Gnann, 2021). This study has developed a
 453 general formulation (the MPS model) through observational data analysis and theoretical
 454 derivation based on the Ponce-Shetty model, unveiling the patterns of variability in different
 455 runoff components at mean annual time scale. Compared to the commonly used Budyko-type
 456 formulations, it can not only estimate mean annual Q and Q_b , but also can depict the variability of
 457 Q_s . Figure 12 shows the estimated mean annual runoff components by the Budyko-type
 458 formulations (equations in the second and fifth rows of Table 1 in this paper). The Budyko-type
 459 formulations also achieve good validation performance, with R^2 greater than 0.95 and RMSE less
 460 than 78 mm. Although the MPS model and the Budyko-type formulations are comparable in
 461 terms of R^2 , especially with almost equal simulation results of Q_s , the MPS model reduced the
 462 RMSE values by 10 mm and 12 mm for estimating Q_b , respectively.



463
 464 **Figure 12.** The observed and simulated mean annual (a) surface flow, (b) baseflow and (c) total
 465 runoff by the Budyko-type formulations in China (red circles) and the CONUS (blue circles).

466 Figure 13 presents the estimation of SFC and BFC in validation periods using the Budyko-type
 467 formulations. The two methods also show highly consistent estimation of SFC , with R^2 of 0.94

468 and RMSE of 0.03. However, the Budyko-type formulations underestimate the *BFC* of most
 469 catchments in China, while the MPS model greatly improves the simulation accuracy of *BFC*.



470

471 **Figure 13.** The observed and simulated (a) surface flow fraction (Q_s/P) and (b) baseflow fraction
 472 (Q_b/P) by the MPS model in China (red circles) and the CONUS (blue circles).

473 In conclusion, the MPS model has comparable capability in simulating Q_s and *SFC* to that of
 474 Budyko-type formulations. Moreover, it outperforms Budyko-type formulations in estimating Q_b
 475 and Q , and reveals superiority in estimating *BFC*. By characterizing runoff components as
 476 functions of available water at corresponding stages with a composite parameter, the MPS model
 477 is more concise in form and eliminates additional and complex parameter computations, thereby
 478 facilitating broader application in large-sample investigations.

479 In addition to precisely quantifying runoff components and the allocation of precipitation, this
 480 model has innovatively attributed the contributions of different factors on the changes of Q_s and
 481 Q_b . Our results show that the variation of Q_s is jointly controlled by P and other factors. P plays
 482 an dominant role in the variation of Q_s in the catchments of the Yangtze River Basin, Southeast
 483 Basin and Pearl River Basin of China and the west coast of the CONUS, where precipitation has
 484 been reported to have undergone significant changes (Li et al., 2021; Mallakpour and Villarini,
 485 2017; Massoud et al., 2020; Xu et al., 2022). This is possibly due to more extreme precipitation
 486 events and summer rainfall in the middle-lower Yangtze River Basin (Ye et al., 2018) and an
 487 increasing trend in the frequency of heavy precipitation over large areas of the CONUS
 488 (Mallakpour and Villarini, 2017). Previous studies reported that the variation of Q in these
 489 regions are dominated by P (He et al., 2022; Huang et al., 2016). Now it seems that P mainly
 490 affects the first allocation stage (Q_s) and consequently change total runoff. The variation of Q_b is
 491 mainly influenced by V_p , indicating that we should pay more attention to the changes of

492 catchment attributes, atmospheric water and energy demand in most catchments when
493 investigating Q_b .

494 Overall, this conceptual model extracted from observed rainfall-runoff data provides a concise,
495 general and effective tool for predicting runoff components, and evaluating their responses to
496 climate and environment under global change.

497 **5.2. Parameter Interpretation**

498 In the MPS model, each runoff component is associated with a parameter that can be
499 interpreted as the upper limit of the remaining portion of available water after it has been
500 partitioned into runoff at each stage. For instance, in the first stage, precipitation is allocated to
501 surface flow and catchment wetting, with W_p representing the upper limit of catchment wetting,
502 which describes the catchment's storage capacity related to soil, topography and so on (Cheng et
503 al., 2023). W_p is influenced by soil properties and available storage capacity, determining the
504 fraction of precipitation that rapidly becomes surface runoff versus what is stored. For the second
505 stage, the available water comes from catchment wetting, which is then allocated to baseflow and
506 vaporization. The parameter V_p is the upper limit of the fraction of wetting returned to the
507 atmosphere as water vapor (Ponce and Shetty, 1995), and is likely responds to subsurface
508 characteristics such as aquifer permeability and geological layering. For instance, in highly
509 heterogeneous aquifers with well-developed preferential pathways (e.g., fractured rock or karst
510 systems), water is rapidly drained toward the stream, leading to a higher efficiency of baseflow
511 production and thus a lower V_p value (as less water is retained for evaporation). Conversely, in
512 catchments with more homogeneous, porous media (e.g., sandy aquifers), water movement is
513 slower and more diffuse, potentially allowing for a greater fraction of stored water to be
514 evaporated, resulting in a higher V_p . For the total runoff, we consider precipitation as the available
515 water competing with evapotranspiration, whose upper limit is represented by the parameter U_p .
516 Similar to V_p in the second stage, U_p can be regarded as a sort of atmospheric water and energy
517 limit (somewhat analogous to potential evapotranspiration) and emerges from the interaction of
518 the available energy, vegetation and other catchment characteristics. To some extent, the MPS
519 model links Q_s and Q_b with Q using P in the first trade-off and V_p in the second trade-off, so that
520 the forms of different runoff components can be unified.

521 Additionally, we compared the distribution of the parameters in the MPS model with that in
522 Gnann (Gnann et al., 2019) and Siva's work (Sivapalan et al., 2011), which did not omit the
523 initial abstraction coefficients λ_s and λ_b . There is a very similar spatial pattern of W_p and V_p in
524 the CONUS. Specifically, high W_p can be seen in the middle of the United States (Great Plains)
525 and the east (southern parts of the Appalachians) (Figure 7(d)), and high V_p can be seen in the
526 middle of the United States (Great Plains) and all southern regions (Figure 7(e)). This, to some
527 extent, illustrates the rationality of the simplification of the original Ponce-Shetty model in
528 describing the spatial variability of runoff components. According to Ponce and Shetty (1995)
529 and Sivapalan et al. (2011), the products $\lambda_s W_p$ and $\lambda_b V_p$ are viewed as the initial abstraction to
530 generate runoff. This definition is reasonable for short-term scales, such as event and annual
531 scales. However, on the multi-annual scale, the catchment maintains a state of water balance and
532 water losses can be disregarded (Han et al., 2020). Hence, simplifying λ to zero is rational to
533 quantify and attribute runoff components and offer a new perspective on the long-term catchment
534 water balance.

535 **5.3. Uncertainties and Future Improvements**

536 It is important to acknowledge several uncertainties in this study. First, the definition of
537 "baseflow" itself introduces uncertainty. Although widely used as a collective term for delayed
538 streamflow components, baseflow encompasses contributions from hydrologically distinct
539 sources such as groundwater drainage, hyporehic exchange, snowmelt, and deeper subsurface
540 leakage-each with distinct origins, timescales, and sensitivities to environmental factors. For
541 instance, groundwater flow and deep leakage are strongly controlled by geological heterogeneity,
542 including the distribution of rock types, porosity, permeability, faults, and fractures (Schiavo et
543 al., 2023). In contrast, snowmelt baseflow, on the other hand, is mainly driven by temperature
544 variations within interannual to decadal climate cycles.

545 The definition of baseflow directly influences the selection of catchment areas. Guided by this
546 macro-scale definition-viewing baseflow as the relatively stable portion of total runoff-we
547 included large catchments in our analysis. While this inclusion may be a source of error, it does
548 not affect the key finding that the MPS model effectively captures the variability of mean annual
549 runoff components across catchments. A sensitivity analysis of the model's performance under

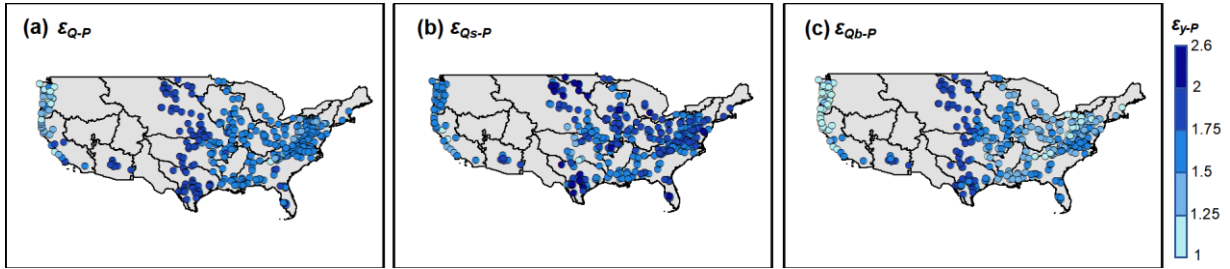
550 different area thresholds is provided in Appendix Table A1. Future studies could combine isotope
551 tracing with hydrological modeling to better quantify the contributions of these different sources.

552 Second, methodological uncertainty arises from the digital filter method (i.e., the Lyne–Hollick
553 algorithm) for baseflow separation. While practical and widely applied, this approach is
554 deterministic and does not explicitly account for uncertainties related to aquifer heterogeneity,
555 such as spatial variability in hydraulic conductivity, preferential flow paths, or geologic structures.
556 Future work could adopt stochastic frameworks such as Monte Carlo simulation by generating
557 multiple realistic realizations of aquifer heterogeneity to obtain more robust and probabilistic
558 baseflow estimates (Schiavo et al., 2023). Additionally, our study did not take into account the
559 spatial heterogeneity of groundwater flow, particularly its preferential pathways through fractures,
560 macropores, or highly permeable sedimentary layers. Event-scale analyses indicate that
561 stormflow volumes and hysteresis patterns covary with subsurface connectivity and its timing.
562 For example, Zuecco et al. (2019) who used graph-theory metrics to quantify connectivity in
563 headwater catchments and linked maximum connectivity to stormflow. While our study operates
564 at mean-annual scales, these findings are consistent with our interpretation that geological
565 heterogeneity and preferential pathways (fractures, karst, macropores) modulate the V_p dispersion
566 and, in turn, the aggregate baseflow fraction. Future work could employ numerical models or
567 distributed hydrological models that explicitly represent geological structures to better capture the
568 effects of preferential flow paths at smaller scales.

569 The sensitivity of runoff to changes in climatic and environmental factors has always been
570 highly anticipated. Schaake (1990) first introduced the concept of climate elasticity coefficients to
571 quantify it, defined as the ratio of the relative change in mean annual runoff to the relative change
572 in climatic factors. Various expressions have been widely applied in evaluating the hydrological
573 response to multi-annual average climate change (Sun et al., 2014; Xu et al., 2014). The only
574 climatic factor in the MPS model is P , so we primarily focuses on the elasticity of runoff
575 components to P (ε), which can be expressed as $\varepsilon_{y-P} = \frac{\partial Q_y}{\partial P} / \frac{Q_y}{P}$, quantifying the percentage of
576 runoff components change caused by 1% change in P .

577 Figure 14 shows elasticities of Q , Q_s and Q_b to P derived from the MPS model in the CONUS.
578 We compare the elasticity distribution of the work conducted by Harman et al. (2011), who did

579 not omit the initial abstraction coefficients λ . In humid catchments with the aridity index of less
 580 than 1 (such as the west coast and eastern regions of the CONUS), the results from both studies
 581 are very close, with elasticity values from 1 to 2. However, the MPS model noticeably
 582 underestimates the runoff sensitivity to P in semi-arid and arid catchments (such as the Great
 583 Plains). This may be due to the error caused by the assumption that λ is a constant when deriving
 584 the MPS model.



585
 586 **Figure 14.** The elasticity of (a) total runoff, (b) surface flow and (c) baseflow to precipitation
 587 derived the MPS model.

588 Additionally, the secondary rainfall processes, such as initial abstraction to generate runoff,
 589 precipitation intensity and seasonality should be considered in these regions, which have been
 590 proven to have a significant impact in attribution analysis (He et al., 2022; Ning et al., 2022;
 591 Zhang, 2015). Moreover, the potential evapotranspiration (E_0), which indicates the impact of
 592 energy constraints (Huang et al., 2019; Wu et al., 2020), is quite significant in arid and semi-arid
 593 catchments and should be taken into account.

594 In this paper, we interpret the parameters (i.e., W_p , V_p and U_p) as a potential upper limit of each
 595 partition stage competing with corresponding runoff components following the annual
 596 Ponce-Shetty model. It is intriguing to discuss whether the connotation of the parameters has
 597 changed from annual to mean annual time scale. On a long-term scale, the initial abstraction
 598 coefficient (i.e., λ_p and λ_W) can be simplified as zero, indicating the loss for generating runoff is
 599 negligible. However, to what extent the initial abstraction coefficient affect precipitation partition
 600 at shorter time scales is still under-determined. The physical and theoretical interpretation of
 601 parameters and their impacts at different time scales are temporarily outside the scope of this
 602 study. However, it is valuable to further research in future work. In addition, the seasonality of
 603 rainfall measures the concentration of precipitation within a year. The more concentrated the
 604 precipitation, the more likely it is to generate surface runoff, resulting in greater intra-annual

605 fluctuations in the BFI and a lower annual BFI. In contrast, in catchments with evenly distributed
606 precipitation, soil water and groundwater are replenished consistently and gradually, leading to
607 relatively stable intra-annual BFI and a higher annual BFI.

608 The MPS model has only one parameter for controlling each runoff component, which is
609 arguably simplified but dependent on calibration, and their physical meaning needs further
610 explanation. We still need to explain the parameters in terms of regional patterns of climatic
611 and/or catchment attributes, meaning that currently this model can only be applied to gauged
612 catchments with runoff observations and challenging to transfer to ungauged basins. Cheng et al.
613 (2022) proposed two machine learning methods to characterize the parameter of the Budyko
614 framework and further employed them in estimating global runoff partition (Cheng et al., 2023).
615 Results show that parameters related to vegetation (such as root zone storage capacity, water use
616 efficiency and vegetation coverage) and climate (such as precipitation depth and climate
617 seasonality) are the primary controlling factors of the parameter. Similar work can be referred to
618 (Chen and Ruan, 2023). These investigations provide priori knowledge for quantitatively linking
619 the parameters of the MPS model to climate forcing and catchment attributes in future work.

620 **6. Conclusion**

621 We developed a general formulation (the MPS model) to estimate mean annual runoff
622 components as a function of available water with a synthetic parameter based on a two-stage
623 partition theory, and validated it over 662 catchments across China and the CONUS with further
624 attribution analysis. The concise MPS model provides more accurate runoff components
625 estimation and innovative attribution, offering new insights to long-term water balance and giving
626 additional superiorities toward making predictions of runoff variation under global change. The
627 main conclusions are as follows:

628 (1) The investigated catchments fit well with the MPS model, with R^2 of 0.86, 0.68 and 0.91 for
629 fitting Q_s , Q_b and Q in China and R^2 of 0.81, 0.44 and 0.80 for fitting Q_s , Q_b and Q in the CONUS,
630 implying the MPS model can well reproduce the spatial variability of different runoff
631 components.

632 (2) The MPS model effectively simulates multi-year runoff components with R^2 exceeding 0.97,

633 and the proportion of runoff components relative to precipitation with R^2 exceeding 0.94. The
634 spatial distribution of the parameters across China and the CONUS is related to that of climate
635 zoning.

636 (3) The MPS model has proved effective in quantifying the variations of runoff components
637 induced by precipitation and environmental factors. The estimated and observed ΔQ_s , ΔQ_b and
638 ΔQ exhibit high consistency, with an R^2 of 0.99 and RMSE of 1.6 mm of ΔQ_s attribution, R^2 of
639 0.90 and RMSE of 16 mm of ΔQ_b attribution and R^2 of 0.91 and RMSE of 42 mm of ΔQ
640 attribution, respectively. The variation of Q_s is jointly controlled by P and environmental factors,
641 while the variation of Q_b is mainly influenced by V_p in most catchments.

642 In general, this study proposes a general formulation for effectively estimating and attributing
643 the mean annual runoff, surface flow and baseflow. The structure is simple with few parameters
644 and clear physical significance. Its reliability has been authenticated, providing new insights for
645 analyzing watershed water resources in changing environments.

646

647 **Author Contribution**

648 Y.H: conceptualization; model development/theoretical derivation; investigation; calculation;
649 formal analysis; visualization; writing original draft.
650 H.Y: conceptualization; model development/theoretical derivation; data curation; writing review
651 & editing; supervision; funding acquisition.
652 C.L.: conceptualization; data analysis; visualization; writing review & editing.

653 **Competing interests**

654 The authors declare that they have no conflict of interest.

655

656 **Appendix**657 Table A1 The coefficient of determination (R^2) and model parameters for the MPS curve fittings under different
658 area thresholds for selecting catchments in China

Area thresholds (km ²)	Number of catchments	R^2			Parameters (mm)		
		Q_s	Q_b	Q	W_p	V_p	U_p
2,000	67	0.85	0.62	0.89	3220	2794	1439
5,000	135	0.84	0.63	0.89	3004	2651	1356
10,000	180	0.84	0.69	0.90	3098	2614	1375
20,000	219	0.85	0.68	0.90	3138	2585	1376
80,000	257	0.85	0.69	0.90	3207	2487	1364
500,000	295	0.85	0.69	0.91	3278	2428	1362

659

660 **Acknowledgments**

661 This research was supported by the National Natural Science Foundation of China (grant no.
662 42041004 and 52309022) and the China National Key R&D Program (grant nos.
663 2021YFC3000202 and 2022YFC3002802).

664 **Data and code Availability**

665 The CAMELS data set is available at <https://ral.ucar.edu/solutions/products/camels>. The
666 hydro-meteorological data of the catchments across China can be obtained from the Zenodo
667 repository via <https://zenodo.org/records/11058118> (Li et al., 2024).

668 **Reference**

669 Addor, N., Newman, A.J., Mizukami, N. & Clark, M.P. (2017). The CAMELS data set: catchment attributes and
670 meteorology for large-sample studies. *Hydrology and Earth System Sciences*, 21(10): 5293-5313.
671 DOI:10.5194/hess-21-5293-2017

672 Al-Ghobari, H., Dewidar, A. & Alataway, A. (2020). Estimation of Surface Water Runoff for a Semi-Arid Area Using RS
673 and GIS-Based SCS-CN Method. *Water*, 12(7). DOI:10.3390/w12071924

674 Beck, H.E., van Dijk, A., Miralles, D.G., de Jeu, R.A.M., Bruijnzeel, L.A., McVicar, T.R. & Schellekens, J. (2013). Global
675 patterns in base flow index and recession based on streamflow observations from 3394 catchments. *Water
676 Resources Research*, 49(12): 7843-7863. DOI:10.1002/2013wr013918

677 Berghuijs, W.R., Larsen, J.R., van Emmerik, T.H.M. & Woods, R.A. (2017). A Global Assessment of Runoff Sensitivity
678 to Changes in Precipitation, Potential Evaporation, and Other Factors. *Water Resources Research*, 53(10):
679 8475-8486. DOI:10.1002/2017wr021593

680 Beven, K.J. & Kirkby, M.J. (1979). A physically based, variable contributing area model of basin hydrology / Un
681 modèle à base physique de zone d'appel variable de l'hydrologie du bassin versant. *Hydrological Sciences
682 Bulletin*, 24(1): 43-69. DOI:10.1080/02626667909491834

683 Budyko, M.I., (1974). Climate and life: English Edited by Miller, D. H. Academic Press, New York.

684 Chen, S. & Ruan, X.H. (2023). A hybrid Budyko-type regression framework for estimating baseflow from climate and
685 catchment attributes. *Journal of Hydrology*, 618. DOI:10.1016/j.jhydrol.2023.129118

686 Cheng, S., Hulsman, P., Koppa, A., Beck, H.E., Cheng, L. & Miralles, D.G., (2023). Global runoff partitioning based on
687 Budyko-constrained machine learning. Zenodo. DOI:<https://doi.org/10.5281/ZENODO.7932122>

688 Cheng, S.J., Cheng, L., Liu, P., Qin, S.J., Zhang, L., Xu, C.Y., Xiong, L.H., Liu, L. & Xia, J. (2021). An Analytical Baseflow
689 Coefficient Curve for Depicting the Spatial Variability of Mean Annual Catchment Baseflow. *Water
690 Resources Research*, 57(8). DOI:10.1029/2020wr029529

691 Cheng, S.J., Cheng, L., Liu, P., Zhang, L., Xu, C.Y., Xiong, L.H. & Xia, J. (2020). Evaluation of baseflow modelling
692 structure in monthly water balance models using 443 Australian catchments. *Journal of Hydrology*, 591.
693 DOI:10.1016/j.jhydrol.2020.125572

694 Cheng, S.J., Cheng, L., Qin, S.J., Zhang, L., Liu, P., Liu, L., Xu, Z.C. & Wang, Q.L. (2022). Improved Understanding of
695 How Catchment Properties Control Hydrological Partitioning Through Machine Learning. *Water Resources*
696 *Research*, 58(4). DOI:10.1029/2021wr031412

697 Choudhury, B.J. (1999). Evaluation of an empirical equation for annual evaporation using field observations and
698 results from a biophysical model. *Journal of hydrology (Amsterdam)*, 216(1-2): 99-110.
699 DOI:10.1016/S0022-1694(98)00293-5

700 de Graaf, I.E.M., Gleeson, T., van Beek, L.P.H., Sutanudjaja, E.H., Bierkens, M.F.P., Hyologie, Landscape functioning, G.
701 & Hyology. (2019). Environmental flow limits to global groundwater pumping. *Nature*, 574(7776): 90-94.
702 DOI:10.1038/s41586-019-1594-4

703 Fan, Y., Li, H. & Miguez-Macho, G. (2013). Global Patterns of Groundwater Table Depth. *Science*, 339(6122): 940-943.
704 DOI:10.1126/science.1229881

705 Ficklin, D.L., Robeson, S.M. & Knouft, J.H. (2016). Impacts of recent climate change on trends in baseflow and
706 stormflow in United States watersheds. *Geophysical Research Letters*, 43(10): 5079-5088.
707 DOI:10.1002/2016gl069121

708 Gnann, S.J., (2021). Baseflow Generation at the Catchment Scale : an Investigation Using Comparative Hydrology.
709 Dissertation/Thesis Thesis.

710 Gnann, S.J., Woods, R.A. & Howden, N.J.K. (2019). Is There a Baseflow Budyko Curve? *Water Resources Research*,
711 55(4): 2838-2855. DOI:10.1029/2018wr024464

712 Hale, C.A., Carling, G.T., Nelson, S.T., Fernandez, D.P., Brooks, P.D., Rey, K.A., Tingey, D.G., Packer, B.N. & Aanderud, Z.T.
713 (2022). Strontium isotope dynamics reveal streamflow contributions from shallow flow paths during
714 snowmelt in a montane watershed, Provo River, Utah, USA. *Hydrological Processes*, 36(1).
715 DOI:10.1002/hyp.14458

716 Hall, F.R. (1968). BASE-FLOW RECESSIONS-A REVIEW. *Water Resources Research*, 4(5): 973-8.
717 DOI:10.1029/WR004i005p00973

718 Han, J.T., Yang, Y.T., Roderick, M.L., McVicar, T.R., Yang, D.W., Zhang, S.L. & Beck, H.E. (2020). Assessing the
719 Steady-State Assumption in Water Balance Calculation Across Global Catchments. *Water Resources*
720 *Research*, 56(7). DOI:10.1029/2020wr027392

721 Han, P.F., Sankarasubramanian, A., Wang, X.S., Wan, L. & Yao, L.L. (2023). One-Parameter Analytical Derivation in
722 Modified Budyko Framework for Unsteady-State Streamflow Elasticity in Humid Catchments. *Water*
723 *Resources Research*, 59(9). DOI:10.1029/2023wr034725

724 Harman, C.J., Troch, P.A. & Sivapalan, M. (2011). Functional model of water balance variability at the catchment
725 scale: 2. Elasticity of fast and slow runoff components to precipitation change in the continental United
726 States. *Water Resources Research*, 47. DOI:10.1029/2010wr009656

727 He, Y., Hu, Y.Y., Song, J.X. & Jiang, X.H. (2021). Variation of runoff between southern and northern China and their
728 attribution in the Qinling Mountains, China. *Ecological Engineering*, 171.
729 DOI:10.1016/j.ecoleng.2021.106374

730 He, Y., Yang, H., Liu, Z. & Yang, W. (2022). A framework for attributing runoff changes based on a monthly water
731 balance model: An assessment across China. *Journal of Hydrology*, 615: 128606.
732 DOI:<https://doi.org/10.1016/j.jhydrol.2022.128606>

733 He, Y., Yang, H. & Li, C. (2025). Long-term variations and regional disparities in baseflow during 1960 – 2021 across
734 China. *Journal of Hydrology*, 663: 134297. DOI:<https://doi.org/10.1016/j.jhydrol.2025.134297>

735 Hellwig, J. & Stahl, K. (2018). An assessment of trends and potential future changes in groundwater-baseflow
736 drought based on catchment response times. *Hydrology and Earth System Sciences*, 22(12): 6209-6224.
737 DOI:10.5194/hess-22-6209-2018

738 Horton, R.E. (1933). The role of infiltration in the hydrological cycle. *Eos, Transactions American Geophysical Union*,
739 14: 446–460.

740 Huang, M.B., Gallichand, J., Dong, C.Y., Wang, Z.L. & Shao, M.G. (2007). Use of soil moisture data and curve number
741 method for estimating runoff in the Loess Plateau of China. *Hydrological Processes*, 21(11): 1471-1481.
742 DOI:10.1002/hyp.6312

743 Huang, T., Yu, D., Cao, Q. & Qiao, J. (2019). Impacts of meteorological factors and land use pattern on hydrological
744 elements in a semi-arid basin. *Sci Total Environ*, 690: 932-943. DOI:10.1016/j.scitotenv.2019.07.068

745 Huang, Z., Yang, H. & Yang, D. (2016). Dominant climatic factors driving annual runoff changes at the catchment
746 scale across China. *Hydrology and earth system sciences*, 20(7): 2573-2587.
747 DOI:10.5194/hess-20-2573-2016

748 Kaleris, V. & Langousis, A. (2017). Comparison of two rainfall-runoff models: effects of conceptualization on water
749 budget components. *Hydrological Sciences Journal-Journal Des Sciences Hydrologiques*, 62(5): 729-748.
750 DOI:10.1080/02626667.2016.1250899

751 L'vovich, M.I., (1979). World water resources and their future. , Washington: American Geophysical Union.
752 DOI:<https://doi.org/10.1029/SP013>

753 Lee, S.H.Y. & Ajami, H. (2023). Comprehensive assessment of baseflow responses to long-term meteorological
754 droughts across the United States. *Journal of Hydrology*, 626. DOI:10.1016/j.jhydrol.2023.130256

755 Li, X., Zhang, K., Gu, P.R., Feng, H.T., Yin, Y.F., Chen, W. & Cheng, B.C. (2021). Changes in precipitation extremes in the
756 Yangtze River Basin during 1960-2019 and the association with global warming, ENSO, and local effects.
757 *Science of the Total Environment*, 760. DOI:10.1016/j.scitotenv.2020.144244

758 Li, Z., Huang, S., Liu, D., Leng, G., Zhou, S. & Huang, Q. (2020). Assessing the effects of climate change and human
759 activities on runoff variations from a seasonal perspective. *Stoch Environ Res Risk Assess*, 34(3-4): 575-592.
760 DOI:10.1007/s00477-020-01785-1

761 Liu, J.Y., Zhang, Q., Feng, S.Y., Gu, X.H., Singh, V.P. & Sun, P. (2019). Global Attribution of Runoff Variance Across
762 Multiple Timescales. *Journal of Geophysical Research-Atmospheres*, 124(24): 13962-13974.
763 DOI:10.1029/2019jd030539

764 Liu, Z., Yang, H. & Wang, T. (2021). A simple framework for estimating the annual runoff frequency distribution
765 under a non-stationarity condition. *Journal of hydrology (Amsterdam)*, 592: 125550.
766 DOI:10.1016/j.jhydrol.2020.125550

767 Lyne, V.D., Hollick, M., (1979). Stochastic time-variable rainfall runoff modelling. In *Hydrology and Water Resources
768 Symposium* (pp. 82–92). Institution of Engineers, Perth, Australia.

769 Mallakpour, I. & Villarini, G. (2017). Analysis of changes in the magnitude, frequency, and seasonality of heavy
770 precipitation over the contiguous USA. *Theoretical and Applied Climatology*, 130(1-2): 345-363.
771 DOI:10.1007/s00704-016-1881-z

772 Massoud, E.C., Lee, H., Gibson, P.B., Loikith, P. & Waliser, D.E. (2020). Bayesian Model Averaging of Climate Model
773 Projections Constrained by Precipitation Observations over the Contiguous United States. *Journal of
774 hydrometeorology*, 21(10): 2401-2418. DOI:10.1175/JHM-D-19-0258.1

775 Milly, P.C.D. & Dunne, K.A. (2002). Macroscale water fluxes 2. Water and energy supply control of their interannual
776 variability. *Water Resour. Res*, 38(10): 24-1-24-9. DOI:10.1029/2001WR000760

777 Morgan, R.P.C., Nearing, M. A. (Eds.). (2011). *Handbook of erosion modeling*. West Sussex: Wiley - Blackwell.

778 Neto, A.A.M., Roy, T., de Oliveira, P.T.S. & Troch, P.A. (2020). An Aridity Index-Based Formulation of Streamflow
779 Components. *Water Resources Research*, 56(9). DOI:10.1029/2020wr027123

780 Newman, A.J., Clark, M.P., Sampson, K., Wood, A., Hay, L.E., Bock, A., Viger, R.J., Blodgett, D., Brekke, L., Arnold, J.R.,
781 Hopson, T. & Duan, Q. (2015). Development of a large-sample watershed-scale hydrometeorological data

782 set for the contiguous USA: data set characteristics and assessment of regional variability in hydrologic
 783 model performance. *Hydrology and Earth System Sciences*, 19(1): 209-223. DOI:10.5194/hess-19-209-2015

784 Ning, T., Feng, Q. & Qin, Y. (2022). Recent variations in the seasonality difference between precipitation and
 785 potential evapotranspiration in China. *International journal of climatology*, 42(7): 3616-3632.
 786 DOI:10.1002/joc.7435

787 Penman, H.L. (1948). Natural evaporation from open water, bare soil and grass. *Proc. R. Soc. London Ser. Math. Phys.*
 788 *Sci.* 193 (1032), 120. DOI: <https://doi.org/10.1098/rspa.1948.0037>

789 [Pimentel, R., Arheimer, B., Crochemore, L., Andersson, J. C. M., Pechlivanidis, I. G. & Gustafsson, D. \(2023\). Which](#)
 790 [Potential Evapotranspiration Formula to Use in Hydrological Modeling World - Wide? Water resources](#)
 791 [research, 59\(5\). DOI:10.1029/2022WR033447](#)

792 Ponce, V.M. & Shetty, A.V. (1995). A CONCEPTUAL-MODEL OF CATCHMENT WATER-BALANCE .1. FORMULATION AND
 793 CALIBRATION. *Journal of Hydrology*, 173(1-4): 27-40. DOI:10.1016/0022-1694(95)02739-c

794 Price, K., Jackson, C.R., Parker, A.J., Reitan, T., Dowd, J. & Cyterski, M. (2011). Effects of watershed land use and
 795 geomorphology on stream low flows during severe drought conditions in the southern Blue Ridge
 796 Mountains, Georgia and North Carolina, United States. *Water Resources Research*, 47.
 797 DOI:10.1029/2010wr009340

798 Roderick, M.L. & Farquhar, G.D. (2011). A simple framework for relating variations in runoff to variations in climatic
 799 conditions and catchment properties. *Water Resour. Res.*, 47(12): n/a. DOI:10.1029/2010WR009826

800 Schaake, J.C., (1990). From climate to flow, in: climate change and U.S. water resources, edited by: Waggoner, P. E.,
 801 chap. 8. John Wiley, New York.

802 Schiavo, M. (2023). The role of different sources of uncertainty on the stochastic quantification of subsurface
 803 discharges in heterogeneous aquifers. *Journal of Hydrology*, 617: 128930.
 804 DOI:10.1016/j.jhydrol.2022.128930

805 SCS, (1972). National Engineering Handbook, section 4. Soil Conservation Service USDA, Washington, DC.

806 Shen, Y. & Xiong, A.Y. (2016). Validation and comparison of a new gauge-based precipitation analysis over mainland
 807 China. *International Journal of Climatology*, 36(1): 252-265. DOI:10.1002/joc.4341

808 Shi, W., Huang, M., Gongadze, K. & Wu, L. (2017). A Modified SCS-CN Method Incorporating Storm Duration and
 809 Antecedent Soil Moisture Estimation for Runoff Prediction. *Water Resources Management*, 31(5):
 810 1713-1727. DOI:<https://doi.org/10.1007/s11269-017-1610-0>

811 Singh, S.K., Pahlow, M., Booker, D.J., Shankar, U. & Chamorro, A. (2019). Towards baseflow index characterisation at
 812 national scale in New Zealand. *Journal of Hydrology*, 568: 646-657. DOI:10.1016/j.jhydrol.2018.11.025

813 Sivapalan, M., Yaeger, M.A., Harman, C.J., Xu, X.Y. & Troch, P.A. (2011). Functional model of water balance variability
 814 at the catchment scale: 1. Evidence of hydrologic similarity and space-time symmetry. *Water Resources*
 815 *Research*, 47. DOI:10.1029/2010wr009568

816 Sun, Y., Tian, F.Q., Yang, L. & Hu, H.P. (2014). Exploring the spatial variability of contributions from climate variation
 817 and change in catchment properties to streamflow decrease in a mesoscale basin by three different
 818 methods. *Journal of Hydrology*, 508: 170-180. DOI:10.1016/j.jhydrol.2013.11.004

819 Troch, P.A., Martinez, G.F., Pauwels, V.R.N., Durcik, M., Sivapalan, M., Harman, C., Brooks, P.D., Gupta, H. & Huxman,
 820 T. (2009). Climate and vegetation water use efficiency at catchment scales. *Hydrological Processes*, 23(16):
 821 2409-2414. DOI:10.1002/hyp.7358

822 Wallace, S., Biggs, T., Lai, C.-T. & McMillan, H. (2021). Tracing sources of stormflow and groundwater recharge in an
 823 urban, semi-arid watershed using stable isotopes. *Journal of Hydrology: Regional Studies*, 34: 100806.
 824 DOI:<https://doi.org/10.1016/j.ejrh.2021.100806>

825 Wang, D. & Wu, L. (2013). Similarity of climate control on base flow and perennial stream density in the Budyko

826 framework. *Hydrology and earth system sciences*, 17(1): 315-324. DOI:10.5194/hess-17-315-2013

827 Wang, H., Liu, J., Klaar, M., Chen, A., Gudmundsson, L. & Holden, J. (2024). Anthropogenic climate change has
828 influenced global river flow seasonality. *Science (New York, N.Y.)*, 383(6686): 1009-1014.
829 DOI:10.1126/science.adi9501

830 Wang, K., Bai, P. & Liu, X. (2025). Three Paradoxes Related to Potential Evapotranspiration in a Warming Climate.
831 *Current climate change reports*, 11(1):6. DOI:10.1007/s40641-025-00203-4

832 Wu, J.W., Miao, C.Y., Duan, Q.Y., Lei, X.H., Li, X.Y. & Li, H. (2019). Dynamics and Attributions of Baseflow in the
833 Semiarid Loess Plateau. *Journal of Geophysical Research-Atmospheres*, 124(7): 3684-3701.
834 DOI:10.1029/2018jd029775

835 Wu, S., Zhao, J., Wang, H. & Sivapalan, M. (2021). Regional Patterns and Physical Controls of Streamflow Generation
836 Across the Conterminous United States. *Water resources research*, 57(6): n/a. DOI:10.1029/2020WR028086

837 Wu, Y.Y., Fang, H.W., Huang, L. & Ouyang, W. (2020). Changing runoff due to temperature and precipitation
838 variations in the dammed Jinsha River. *Journal of Hydrology*, 582. DOI:10.1016/j.jhydrol.2019.124500

839 Xu, F., Zhou, Y.Y. & Zhao, L.L. (2022). Spatial and temporal variability in extreme precipitation in the Pearl River Basin,
840 China from 1960 to 2018. *International Journal of Climatology*, 42(2): 797-816. DOI:10.1002/joc.7273

841 Xu, X.Y., Yang, D.W., Yang, H.B. & Lei, H.M. (2014). Attribution analysis based on the Budyko hypothesis for detecting
842 the dominant cause of runoff decline in Haihe basin. *Journal of Hydrology*, 510: 530-540.
843 DOI:10.1016/j.jhydrol.2013.12.052

844 Yang, H.B., Qi, J., Xu, X.Y., Yang, D.W. & Lv, H.F. (2014). The regional variation in climate elasticity and climate
845 contribution to runoff across China. *Journal of Hydrology*, 517: 607-616. DOI:10.1016/j.jhydrol.2014.05.062

846 Yang, H.B., Yang, D.W., Lei, Z.D. & Sun, F.B. (2008). New analytical derivation of the mean annual water-energy
847 balance equation. *Water Resources Research*, 44(3). DOI:10.1029/2007wr006135

848 Yang, W.T., Long, D. & Bai, P. (2019). Impacts of future land cover and climate changes on runoff in the mostly
849 afforested river basin in North China. *Journal of Hydrology*, 570: 201-219.
850 DOI:10.1016/j.jhydrol.2018.12.055

851 Yao, L.L., Sankarasubramanian, A. & Wang, D.B. (2021). Climatic and Landscape Controls on Long-Term Baseflow.
852 *Water Resources Research*, 57(6). DOI:10.1029/2020wr029284

853 Ye, X., Xu, C., Zhang, D. & Li, X. (2018). Variation of Summer Precipitation and Its Connection with Asian Monsoon
854 System in the Middle-lower Yangtze River Basin. *Scientia Geographica Sinica*, 38(7): 1174-1182.

855 Yin, J.B., Gentine, P., Zhou, S., Sullivan, S.C., Wang, R., Zhang, Y. & Guo, S.L. (2018). Large increase in global storm
856 runoff extremes driven by climate and anthropogenic changes. *Nature Communications*, 9.
857 DOI:10.1038/s41467-018-06765-2

858 Zhang, D., (2015). On the effects of seasonality of precipitation and potential evapotranspiration on catchment
859 hydrologic partitioning., Tsinghua University, Beijing, China, p. 150. pp.

860 Zhang, J.L., Zhang, Y.Q., Song, J.X. & Cheng, L. (2017). Evaluating relative merits of four baseflow separation methods
861 in Eastern Australia. *Journal of Hydrology*, 549: 252-263. DOI:10.1016/j.jhydrol.2017.04.004

862 Zheng Mingguo, S.L. (2014). Recent change of runoff and its components of baseflow and surface runoff in response
863 to climate change and human activities for the Lishui watershed of southern China (in Chinese).
864 *Geographical Research*, 33(02): 237-250.

865 Zuecco, G., Rinderer, M., Penna, D., Borga, M. & van Meerveld, H.J. (2019). Quantification of subsurface
866 hydrologic connectivity in four headwater catchments using graph theory. *The Science of the total
867 environment*, 646:1265-1280. DOI:10.1016/j.scitotenv.2018.07.269